QUANTIFICATION OF ULTRASONIC SHEAR WAVE SCATTERING FROM AN ELEMENT OF A COMPOUND SCATTERER IN A BONDED PLATE VIA WAVEFIELD IMAGING

A Thesis
Presented to
The Academic Faculty

By

Carson T. Maki

In Partial Fulfillment
of the Requirements for the Degree
Master of Science in the
George W. Woodruff School of Mechanical Engineering

Georgia Institute of Technology

August 2017

QUANTIFICATION OF ULTRASONIC SHEAR WAVE SCATTERING FROM AN ELEMENT OF A COMPOUND SCATTERER IN A BONDED PLATE VIA WAVEFIELD IMAGING

Approved by:

Dr. Laurence Jacobs, Advisor
George W. Woodruff School of Mechanical Engineering
Georgia Institute of Technology

Dr. Jennifer E. Michaels, Co-Advisor
School of Electrical and Computer Engineering
Georgia Institute of Technology

Dr. Karim Sabra
George W. Woodruff School of Mechanical Engineering
Georgia Institute of Technology

Dr. Massimo Ruzzene
School of Aerospace Engineering
Georgia Institute of Technology

Date Approved: May 2, 2017

But remember this... airplanes are not tools for war. They are not for making money.

Airplanes are beautiful dreams. Engineers turns dreams into reality.

-Hayao Miyazaki

To my family, without whom my life would be quite normal.

ACKNOWLEDGEMENTS

I would like to thank my advisor, Dr. Jennifer Michaels, for her guidance throughout this research. Her dedication to her students and her attention to detail has made my experience in the QUEST Lab both enjoyable and challenging. Her tutelage has afforded me opportunities and personal growth experiences for which I will always be grateful.

I would also like to thank the members of my committee, Dr. Laurence Jacobs, Dr. Karim Sabra and Dr. Massimo Ruzzene for their support throughout my academic and research endeavors. I am especially grateful to Dr. Sabra for his insightful and enthusiastic tutelage in acoustics, a course that remains one of my favorites to this day.

Thank you to my friends and colleagues, Yu Weng and Westin Williams, in the QUEST Laboratory for their insight, support, and frequent discussions concerning both research and the mundane. Your help with technical and personal matters alike has pushed me along at times when I needed a nudge. I would also to thank all of my friends, peers, and professors at the Georgia Institute of Technology, who have made my experiences here immensely rewarding and unforgettable.

To my family, whose love and support throughout my life has molded me into the person I am today, I thank you. I owe my most sincere gratitude to my parents, Shawn and Karla, sister Mekenzie, and brother Austin. Whether they know it or not, they all have had an immeasurable impact on my life and have always been the base upon which my character is built.

This project was funded by the Air Force Research Laboratory (AFRL) under Contract Nos. FA8650-10-D-5210 and FA8650-15-D-5231.

TABLE OF CONTENTS

LIST OF TABLES

LIST OF FIGURES

SUMMARY

The objectives of this thesis are to acquire high quality 3-D wavefield data via wavefield imaging and develop, describe and demonstrate analysis techniques that quantify the scattering of angle-beam ultrasonic waves from an element of a compound scatterer in bonded plates. Improved understanding of ultrasonic scattering for the case of buried defects in layered specimens is important for the development of nondestructive evaluation (NDE) methods, particularly in the aerospace industry. Angle-beam techniques are often used in industry to detect and characterize defects in plate-like structures; moreover, layered plates are also used in industry and can result in more complicated scattering. Scattering from through-holes, on which significant experimental work has already been done, is particularly important because cracks tend to form around fastener holes due to high stress concentrations. In the case that a crack does form at a through-hole, the combination of through-hole and crack-like defect(s) creates a compound scatterer, implying that the resulting scattered wavefield is composed of two or more contributing elements.

Experimental processes for acquiring wavefields using a laser Doppler vibrometer, which measures the out-of-plane motion of ultrasonic waves on the surface of a specimen and allow for the visualization and characterization of propagating waves, are presented. Wavefields are obtained for compound scatterers with different defect geometries to investigate the effects of defect orientation and size on scattering quantification.

Methods are described for processing acquired wavefields and obtaining radial energy curves, which are used to quantify buried defect scattering in layered plates. Wavefield baseline subtraction is discussed and applied to current and reference wavefield data; however, it is shown that wavefield baseline subtraction fails to yield useful residual wavefields for defect scattering quantification. An alternative approach for segregating an element (defect) from a compound (through-hole plus defect) scatterer is developed and demonstrated. Four methods for generating radial energy curves are discussed and implemented on ac-

quired data. One method accumulates energy in the frequency-wavenumber domain, while the other three do so in the time-space domain; advantages and disadvantages of operating in each domain are discussed.

Each method is demonstrated in the analysis of data acquired from a series of experiments for a range of defect conditions. The results show that each radial energy calculation method presented in this thesis provides useful scattering information for incremental scattering scenarios. Time-space radial energy calculations over a time window prove to be the most useful method discussed in this thesis for quantifying defect scattering over multiple scattering frames. Although the methods for segregating and quantifying buried defect scattering are applied to angle-beam wavefield measurements, the methodology presented in this thesis is generally applicable to any set of wavefield data containing a scatterer of interest within a compound scatterer.

CHAPTER 1
INTRODUCTION AND BACKGROUND

This chapter presents a brief background describing the importance of understanding ultrasonic scattering from defects and factors motivating this research. Then, research goals are outlined, which focus on the design and fabrication of two-layered isotropic plate specimens and the analysis techniques used to investigate scattering from features of interest within the first layer of the specimens. Particular attention is paid to quantifying scattering from buried defects placed at two different orientations and for different defect geometries. Finally, the structure of the remaining chapters of this thesis is summarized.

1.1 Background and Motivation

Ultrasonic nondestructive evaluation (NDE), which uses high-frequency elastic waves to evaluate materials without compromising their integrity, refers to a family of techniques that are frequently applied for detecting and characterizing defects in aerospace materials [1]. Because of its potential for high-fidelity defect detection in a variety of applications, ultrasonic NDE research has largely focused on ultrasonic wave scattering from defects; e.g., understanding the scattering behavior of fatigue cracks emanating from fastener holes in aluminum structural components [2].

Angle-beam ultrasonic NDE uses an angled wedge to inject bulk waves into the material, which is particularly useful for far-surface defect interrogation. Ultrasonic NDE techniques using angle-beam wedges coupled to piezoelectric transducers have also been utilized in measuring the depth of surface-breaking cracks [3] and for in situ sizing of fastener hole cracks [2]. Both of these studies focused on defect characterization whereas the scattered wavefield itself has also been of interest; Zhang *et. al.* investigated the effect of crack roughness on defect scattering for longitudinal bulk waves [4] and Kummer *et.*

al. considered the effect of various fastener hole fill conditions on shear wave scattering [5]. However, these works were limited to monolithic metallic specimens. Feasibility studies on evaluating aluminum-aluminum bonded specimens using ultrasonic NDE have been discussed [6], but there exists little experimental data reported on bulk wavefield scattering in bonded plates with fastener holes. Instead, much of the reported research on angle-beam ultrasonic NDE considers analytical models with simple defect geometries.

It is important to detect and characterize buried defects emanating from through-holes in bonded plate-like structures for aerospace applications. The depth of the buried defect may be much greater than the size of the defect itself; the relatively small size of defects of interest necessitates high-frequency ultrasound for detection whereas the defect's corresponding depth renders guided wave methods [7, 8] less useful. Ultrasonic wavefield imaging combined with signal processing can be applied to angle-beam shear waves propagating in simple plates with through-holes and far-surface notches to characterize the scattered wavefield from known defects. Understanding scattering from known defects is important for improving nondestructive evaluation methods that can be applied to characterize cracks emanating from fastener holes.

1.2 Research Goals and Contributions

This research primarily considers the development and implementation of methods for analyzing ultrasonic scattering from an element of a compound scatterer in two-layer isotropic plates. The data acquired and information gained from implementing the methods developed as a result of this work provide a better understanding of the behavior of ultrasonic scattering from buried defects, which may be used to improve ultrasonic NDE methods. Perhaps more importantly, data acquired during this work provide high quality experimental results by which future ultrasonic wave propagation models can be validated. In this thesis, a set of methodologies for segregating and quantifying scattering from an element of a compound scatterer from the full scattering wavefield are presented and applied to

acquired angle-beam wavefield data. Although the methods may be applied to any 3-D wavefield measurements, they are applied here to notches with known orientations and geometries emanating from through-holes at the far surface of the top layer of a bonded specimen.

1.3 Thesis Organization

The remainder of this thesis is organized as follows: Chapter 2 introduces the main topics pertinent to this research in more detail and provides a literature review of previous research efforts in the areas of angle-beam NDE, ultrasonic wavefield imaging, and ultrasonic scattering quantification. Research objectives are presented in the context of prior research. In Chapter 3, experimental procedures for measuring wavefields are described, layered plate specimen design and fabrication is discussed, and a summary of experiments considering the effects of defect orientation and size on ultrasonic scattering is presented. A variety of wavefield measurements in both the Fourier and time-space domains are presented and used to motivate the need for additional signal processing for conditioning the data for scattering analyses. Chapter 4 discusses in detail the various signal processing techniques applied to acquired data specifically in the Fourier domain. Although the majority of such processing is used to condition the data for scattering analyses, a directional filtering method is presented and implemented to demonstrate a tool for segregating scattered waves from incident waves. For certain instances of through-hole and notch scattering, spatial windowing is used in conjunction with other presented filtering methods to segregate notch scattering from through-hole scattering. In Chapter 5, multiple scattering analysis methods are discussed and implemented. All presented methods utilize radial interpolation whereas only one of them is calculated in the Fourier domain. The advantages and disadvantages of each method, interesting observations of presented data, and concluding remarks and recommendations for future work are presented in Chapter 6.

CHAPTER 2
LITERATURE REVIEW

The purpose of this chapter is to introduce and discuss previous research related to angle-beam ultrasonic testing, wavefield imaging, and analysis techniques of ultrasonic waves in plates. It includes a brief summary of the fundamental equations governing ultrasonic wave propagation and describes the types of waves typically found in plate-like structures. Nondestructive evaluation (NDE) is defined and some techniques particular to ultrasonic NDE and angle-beam testing are presented. Ultrasonic wavefield imaging is presented as an effective experimental tool for measuring wave propagation on the surface of a material. A review of research efforts to quantify ultrasonic scattering from through-holes and, more importantly, crack-like defects and notches is provided. Finally, the work covered in this thesis is put into context in relation to concepts and prior work covered in this chapter, and the research objectives are outlined in the established context.

2.1 Ultrasonic Wave Propagation

Ultrasonic wave propagation theory was established as early as the 19th century [9]. This era of discovery and solutions for both ultrasonics and engineering as a whole produced several principles and technical advances upon which modern-day ultrasonics research is built. Guided and bulk waves are used extensively in modern ultrasonic NDE methods for a variety of geometries of elastic solids.

2.1.1 Elastic Wave Equation

The elastic wave equation governs elastic wave propagation including bulk waves, which can exist as one of two modes: longitudinal, whose periodic compression and rarefaction stresses are parallel to the direction of wave propagation, and transverse, which are com-

monly referred to as shear waves due to their shearing wave motion [9]. Although local particles behave differently according to their mode, both types of particle displacements are expressed as a three dimensional particle vector,

$$\mathbf{u} = \begin{bmatrix} u_x(x,y,z,t) \\ u_y(x,y,z,t) \\ u_z(x,y,z,t) \end{bmatrix}, \tag{2.1}$$

where u_x, u_y, and u_z, are particle displacements in the x, y, and z directions, respectively. Furthermore, each three-dimensional particle displacement is a function of time, t.

The particle displacement for homogeneous, isotropic elastic media in the absence of body forces can be expressed mathematically in terms of the longitudinal and shear wave speeds, c_l and c_s, respectively, using Navier's equation:

$$\frac{\partial^2 \mathbf{u}}{\partial t^2} = c_l^2 \nabla(\nabla \cdot \mathbf{u}) - c_s^2 \nabla \times (\nabla \times \mathbf{u}). \tag{2.2}$$

The longitudinal and shear wave speeds can be expressed in terms of the Lamé constants, λ and μ, and the material density, ρ:

$$c_l = \sqrt{\frac{\lambda + 2\mu}{\rho}}, \tag{2.3}$$

$$c_s = \sqrt{\frac{\mu}{\rho}}. \tag{2.4}$$

The Lamé constants describe the linear stress-strain relation in isotropic materials.

The elastic wave equation in Eq. (2.2) can be solved for an infinite medium using a

plane wave solution. A three-dimensional harmonic plane wave solution is assumed,

$$\mathbf{u}(\mathbf{x}, t) = \mathbf{A} \exp[jk(\mathbf{n} \cdot \mathbf{x} - ct)], \tag{2.5}$$

where the vector $\mathbf{A}$ describes the magnitude and direction of the particle displacement, $\mathbf{k}$ is the wavenumber vector, $k = |\mathbf{k}|$ is the wavenumber, and $\mathbf{n}$ is a unit vector in the direction of propagation. Such a plane wave solution describes both longitudinal and shear bulk wave modes [1]:

$$\mathbf{k}_{l,s} = \begin{bmatrix} k_x \\ k_y \\ k_z \end{bmatrix}, |\mathbf{k}_{l,s}| = \frac{\omega}{c_{l,s}} = \frac{2\pi f}{c_{l,s}}. \tag{2.6}$$

Considering only the real component of the three-dimensional plane wave and substituting $c = \omega/k$ yields

$$\mathbf{u} = \mathbf{A} \cos(k\mathbf{x} \cdot \mathbf{n} - \omega t). \tag{2.7}$$

The solution in Eq. (2.7) is useful because plane waves behave intuitively and present relevant wave propagation information in a compact fashion. However, this solution is valid only for a sufficiently large medium (i.e., elastic waves do not interact with boundaries). In many cases, media of interest in ultrasonic NDE do not meet this requirement and thus the planar solution for the elastic wave equation may not be useful. For example, Hamidzadeh *et al.* consider the problem of a harmonic oblique point force on a half-space, for which a plane wave representation of the resulting elastic wavefield is not a valid solution; instead, the authors provide an analytical solution for the frequency response of an arbitrary point on the surface of a half-space due to a harmonic vertical point force [10].

Surface acoustic waves (SAWs) form and propagate along interfaces separating two media [9]. Rayleigh waves constitute a particular class of SAWs that propagate along the

free surface of a semi-infinite solid and whose amplitude exponentially decays into the bulk of the solid. In practice, Rayleigh waves are observed along the interface between a solid and a sufficiently rarefied medium, such as air [11]. Bulk waves incident on an interface at the second critical angle convert to Rayleigh waves and propagate along that interface in elliptical orbits [12]. Rayleigh waves propagate along the material interface at velocity c_r, which is related to the shear wave velocity, c_s, by the well-known approximation

$$\frac{c_r}{c_s} = \frac{0.87 + 1.12\nu}{1 + \nu}, \tag{2.8}$$

where ν is the Poisson's ratio for the solid [11].

In most cases, and particularly in the case of ultrasonic NDE, propagating waves will interact with a boundary. Wave interaction with a boundary can yield reflection, transmission, surface acoustic waves, refraction, mode conversion of the propagating wave or any combination of the aforementioned results. Shull explains in detail the various characteristics of reflected and transmitted waves at an interface [9]. Bulk waves in solids have two modes of propagation: longitudinal and shear. Shear waves have two polarizations, which are typically referred to as shear horizontal and shear vertical. Bulk waves interacting with an interface potentially generate a reflected and transmitted wave depending on the impedance mismatch across the interface and the angle of incidence. Since each incident wave has two modes of propagation, as many as four transmitted and reflected waves can be generated when a wave interacts with an interface.

The relation between incident and transmitted wave angles is governed by Snell's law,

$$\frac{\sin\theta_i}{c_i} = \frac{\sin\theta_r}{c_r}, \tag{2.9}$$

where θ_i and c_i are the angle of incidence and wave speed in the first material and θ_r and c_r are the angle of refraction and wave speed in the second, refracting material. In the context of Snell's law, a critical angle is the incident angle for which incident wave energy

is refracted such that transmitted energy is bound to and propagates along the interface between the two media. This occurs when the first medium has a wave speed less than that of the second medium and the angle of refraction is $\theta_r = 90°$. There are two possible critical angles for bulk waves (i.e., one for each mode of propagation). Waves incident at the first critical angle will refract such that longitudinal waves are bound to the interface and shear waves refract into the bulk; beyond the second critical angle, incident waves are either totally internally reflected and all incident wave energy transfers to the reflected modes [9] or are bound to the interface as a Rayleigh wave. Mode conversion can also occur with shear vertical waves since they exhibit particle displacement that is oblique to the interface, so a component of the displacement normal to the interface can excite a longitudinal mode.

2.1.2 Types of Ultrasonic Waves in Plates

Bulk wave propagation, where the wavelength of the propagating wave is small relative to the thickness of the medium, has been discussed in the context of the elastic wave equation in homogeneous, isotropic solids. The density and Lamé constants of the material in which the bulk wave propagates determine the velocity of the traveling wave as expressed in Eq. (2.3) and Eq. (2.4). Furthermore, the bulk wave propagation direction and wave speed in plates are defined by the wavenumber vector and frequency whereas wave interactions at an interface (i.e., reflection, refraction, and mode conversion) are governed by Snell's Law [9].

Guided waves are not utilized in this work but are covered here for the sake of establishing context for the use of bulk waves. Rayleigh waves are considered guided waves because they are bound to an interface. Although Rayleigh waves are sometimes used for surface defect interrogation, they are not of particular interest for this work. Lamb waves, a class of guided waves typically referred to as plate waves, are an infinite set of modes that can form when incident waves interact with two parallel free surfaces of a bounded solid and produce multiple reflected bulk waves due to mode conversion. This process repeats

at each free surface, and the reflected bulk waves generate resonances that form symmetric (S_n) and antisymmetric (A_n) modes [9]. Lamb waves are thus bound to plate surfaces in which the waves propagate; their propagation characteristics are a function of λ, μ, ρ, and h, the plate thickness. The properties of the S_0 and A_0 modes change as the ratio of plate thickness to wavelength increases; in fact, Viktorov shows that both S_0 and A_0 modes transfer to Rayleigh modes bound to both free-surfaces of the plate as $k_L h \to \infty$, where k_L is the wavenumber of a Lamb wave and h is the thickness of the plate [11]. Lamb waves are useful in the ultrasonic testing community because they propagate with cylindrical rather than spherical spreading loss and can thus propagate long distances with sufficiently large amplitudes for defect detection.

Lamb waves are also dispersive, meaning that their phase velocity is dependent on frequency. The well-known dispersion curves for both the symmetric and antisymmetric modes can be found in many references [9, 6] and illustrate the dependence of Lamb wave velocity on the frequency-thickness product. Lamb wave dispersion can be leveraged to detect shifts in wavenumber as plate waves interact with free surfaces in composites caused by delaminations [13].

2.2 Nondestructive Evaluation

According to the American Society of Nondestructive Testing, "Nondestructive Testing (NDT) [NDE] is the process of inspecting, testing, or evaluating materials, components or assemblies for discontinuities, or differences in characteristics without destroying the serviceability of the part or system." [14]. NDE encompasses a variety of methods used to determine the material properties, quality, and integrity of a specimen: primary methods include radiographic inspection, magnetic particle inspection, eddy current testing, and ultrasonic inspection. Any one or combination of these techniques may ascertain information from a specimen in a nondestructive manner. Ultrasonic testing (UT) is among the safest techniques, allows for both surface and subsurface inspections, and is applicable to

a variety of materials and industries; thus, it is currently one of the most widely used NDE methods.

2.2.1 Ultrasonic NDE

Ultrasonic NDE is used to determine weld quality, infrastructure integrity, material defects, and more in petrochemical, manufacturing, aerospace, and other industries [15]. In UT, a transducer transforms a voltage pulse into a mechanical vibration that results in a propagating ultrasonic wave. The transducer emitting the wave is placed on the specimen under inspection and the wave propagates through the specimen. The traveling wave is modulated or scattered, depending on the material properties and defects of the specimen, and the resulting wave information is received and converted back into a voltage signal via mechano-electrical transduction. There are two basic types of transmission-reception techniques: pitch-catch and pulse-echo. The pitch-catch method requires a second transducer to receive the signals sent from the transmitting transducer whereas in the pulse-echo method the transmitted signal reflects back to and is received by the transmitting transducer. Either method may be applied to determine the thickness and material properties of a specimen, flaws and delaminations and their shape, size and composition, and behavior of layered materials [9]. For example, rectilinear scans that utilize air-coupled or water-submersed transducers in pulse-echo or pitch-catch configurations can be used to determine anisotropic material integrity, as individual layer delaminations in composites can be characterized by their scattering behavior [16].

2.2.2 Angle-Beam Ultrasonic NDE

Angle-beam ultrasonic NDE utilizes an angle-beam probe to inject ultrasonic waves into a material at an angle oblique to the surface. Angle-beam probes are composed of piezoelectric transducers and acrylic wedges designed to inject ultrasonic waves into a specimen at designated angles. Typically a longitudinal transducer is mounted on the wedge whose

angle is designed to generate a specific refracted angle in a specific material (e.g., 45° in steel). The angle of refraction must be recalculated via Snell's Law when using angle-beam wedges for materials other than the specified reference material (often steel). Angle-beam probes often are used to produce shear-dominant waves in specimens by fixing the angle of incidence to exceed the first critical angle.

Angle-beam probes are typically used on plates to produce bulk waves that propagate at a known angle towards a potential defect. Angle-beam bulk waves propagate through the plate and reflect from the plate surfaces in a series of skips, also referred to as V-paths, where a skip is the sound path from one surface to another and back to the incident surface. Due to the nature of bulk wave propagation, angle-beam inspection allows subsurface defect detection and bulk material characterization and is therefore commonly used in weld inspection [15] and has been applied to characterize plates with surface breaking cracks [3], rough crack-like defects [4], through-holes with varying fill conditions [5], and cracks originating from fastener holes [2].

2.2.3 Ultrasonic Scattering

There is a significant amount of work on theoretically analyzing ultrasonic scattering from various geometrical features such as cylinders and cracks. Shah *et al.* utilized a hybrid technique combining a multipolar representation of the scattered field and the finite-element method to investigate the scattering of longitudinal, shear, and Rayleigh waves by a crack [17]. Aldrin and Knopp [18] implemented a finite element model of angle-beam shear waves incident on a through-hole with a notch combined with spiral head-wave detection to detect notches at various orientations. Aldrin *et al.* [19] developed a 3-D analytical model for angle-beam shear wave scattering from a cylindrical cavity in an infinite elastic medium with the motivation to aid through-hole inspection with emanating cracks.

Scattering from Through-Holes

Ultrasonic scattering from cylindrical features (e.g., through-holes, fastener holes) in homogeneous isotropic media can be described in the context of acoustic cylindrical scattering, which can be expressed as

$$p_s(r,\theta,\omega) = \sum A_n(\omega)\mathrm{H}_n^{(1)}(kr)\mathrm{e}^{jn\theta} \tag{2.10}$$

where k is the wavenumber, r is the radial distance from the scatterer, and $\mathrm{H}_n^{(1)}$ is the Hankel function of the first kind; the linear superposition of incident and scattered waves comprise the entire scattered wavefield,

$$p_t(r,\theta,\omega) = p_i(r,\theta,\omega) + p_s(r,\theta,\omega), \tag{2.11}$$

and a cylindrical scatterer can be modeled as either a perfect or a penetrable scatterer. Analytical solutions to plane harmonic shear horizontal wave scattering from cylindrical geometries in an infinite medium have been present in the UT community since the 1970s [20, 21]. A cylindrical scatterer such as a fastener hole can be modeled as a penetrable scatterer since imperfect impedance and boundary conditions will result in both reflected and transmitted wave energy. Theoretically, through-holes with fill conditions such that the impedance is matched (or close to matched) across the boundary will yield very little reflected wave energy as the majority of incident wave energy is transmitted. Conversely, fill conditions that result in significantly different impedances across the boundary will yield high reflection wave energy and little transmission energy. It is important to note that these analytical modeling techniques assume the medium is infinite or semi-infinite (e.g., plate boundaries are not considered) and that the scatterer is a perfectly cylindrical (i.e., contains no deformations or defects). Kummer *et al.* experimentally investigated the effects of varying through-hole fill conditions of a homogeneous isotropic aluminum 6061

plate [5].

Scattering from Notches

Ultrasonic scattering from crack-like defects has been a source of primary interest in the UT community for many years because of the need for defect detection and characterization in ultrasonic NDE. Defects such as cracks or slots can form in a multitude of ways, but the formations of most interest in NDT and NDE are surface-breaking cracks. Scattering from surface-breaking cracks was studied in the early 1980s by analyzing a series of boundary-value problems and investigating the scattering of longitudinal and shear waves in the frequency domain for homogeneous, isotropic, linearly elastic media [22]. Finite difference schemes were used to evaluate similar scattering phenomena in the time domain, and the numerical results were confirmed with subsequent experiments [23]. Zhang and Achenbach expanded on this work by including numerical analyses for far field scattering from inclined surface-breaking cracks [24].

Some work has also been done to analyze buried cracks. However, due to the complexity of the scattering wavefield, the majority of such work is confined to modeling [18, 19] and numerical [17] solutions, especially for compound scattering situations (i.e., a crack-like defect emanating from a through-hole). Darmon *et al.* developed a system model for diffraction response from crack-like defects based on the Physical Theory of Diffraction, which is a combination of Kirchhoff's Approximation and Geometric Theory of Diffraction [25]. Further modeling efforts have been pursued based on a range of semi-analytical approaches to develop parametric models for crack-like defect diffraction and response in ultrasonic NDT systems: Kirchhoff approximation, Geometric Theory of Diffraction (GTD), and Separation of Variables (SOV) [26, 27]. The (Fresnel) Kirchhoff approximation is a method for analytically expressing the diffraction of a spherical wave via derivation of the homogeneous wave equation using Green's identities. Although originally developed for electromagnetic waves, it is typically utilized in numerical analyses of mechanical wave

diffraction. GTD also is an electromagnetic wave technology applied to the use of high-frequency ultrasound scattering; it leverages near-field responses and diffracted rays to determine the relative amplitude and phase for all directions radiating from the diffracting point. SOV is a common analytical technique applied to solve linear, homogeneous PDEs, in this case the multi-dimensional elastic wave equation.

As alluded to previously, the bulk of the effort on crack-like defect characterization is concentrated in numerical and analytical modeling. A considerable amount of modeling work has already been done on surface-breaking crack-like defects, and the remaining problems of interest, such as scattering from buried cracks emanating from a through-hole, require much more computational resources than is currently practical. Furthermore, few experimental studies have been published due to the difficulty of detecting and quantifying buried defect scattering from a compound scatterer.

2.3 Ultrasonic Wavefield Imaging

Ultrasonic wavefield imaging is the measurement of wave motion on a specimen surface, typically on a two-dimensional rectilinear grid, resulting from a fixed source: the resulting data are three-dimensional (time and two spatial dimensions). Recent developments in technology have made wavefield imaging a viable procedure for damage detection and characterization as well as for validation of numerical modeling and simulations [27]. In this section, acquisition methods, formatting and interpretation techniques, and processing methods for ultrasonic wavefield imaging are discussed.

2.3.1 Acquisition Methods

Typically, ultrasonic wavefields are imaged using a scanning (mirror-based or scanner-based) laser Doppler vibrometer (LDV), which measures out-of-plane displacements on the specimen over a two-dimensional rectilinear grid. Such acoustic wavefields are also imaged via point-wise LDVs or air-coupled ultrasonic transducers (AUT). Both XYZ trans-

lation stage-mounted LDV and AUT scans have been applied to bulk waves [28] and guided waves [29]. As mentioned before, Kummer *et al.* investigated the effect of fill conditions on bulk wave scattering from fastener holes using point-wise LDV, translation stage scanning to image the scattering wavefield [5]. In the case of guided waves, Chen *et al.* provided LDV scan data of scattering of guided waves from notches [7], Fromme and Sayir utilized LDV scans to detect cracks emanating from rivet holes using guided waves [8], and Liu *et al.* used air-coupled transducers to generate and receive Lamb waves for detection of delaminations in quasi-isotropic composite beams [30]. Although some work has been done to collect wavefield imaging data of bulk wavefields, there are many more published results for wavfield imaging of guided waves. Higher temporal and spatial bandwidth requirements for bulk wave measurements at frequencies typically used for NDE are two determining factors for the prevalence of guided wave data and relative lack of bulk wave data.

2.3.2 Formatting and Interpreting Wavefield Data

Ultrasonic data are commonly presented in three formats: A-scans, B-scans, and C-scans. Wavefield data in this thesis are defined in three-dimensions as a function of time and space: $w(x, y, t)$, whose values describe the out-of-plane surface displacement due to ultrasonic wave propagation at position (x, y) and time t. Because most relevant data in this thesis are acquired by wavefield imaging via laser Doppler vibrometry [28], A-, B-, and C-scans in this context are defined somewhat differently from their traditional forms.

In the context of this thesis, A-scans are surface displacement signals at a single point over a time window resulting in a one-dimensional set of data, $w(t)$. A-scans are useful for checking transducer and system functionality by inspecting temporal and spectral content. B-scans are a set of A-scans along a spatial line over a time window. Two-dimensional slices of data, $w(r, t)$, from three-dimensional wavefields, $w(x, y, t)$, are also referred to as B-scans. Any two-dimensional spatial presentation of data, $f(x, y)$, is referred to as a C-

scan. If the spatial presentation is the wavefield at a specific time, $w(x, y, t_0)$, it is usually referred to as a snapshot or frame.

2.3.3 Frequency-Wavenumber Analysis

Frequency-wavenumber analysis refers to wavefield processing algorithms that are implemented in either the 2-D (k_r, ω) or 3-D (k_x, k_y, ω) Fourier domains. Many signal processing applications are implemented in the Fourier domain; one example is mode separation in guided wavefield imaging data [31]. The 3-D Fourier transform, $W(k_x, k_y, \omega)$, of C-scan data, $w(x, y, t)$, is given by

$$W(k_x, k_y, \omega) = \int\int\int w(x, y, t)\mathrm{e}^{-j(\omega t - k_x x - k_y y)}\mathrm{d}x\mathrm{d}y\mathrm{d}t, \tag{2.12}$$

where k_x and k_y are wavenumber components in the x and y directions and ω is the angular frequency.

Frequency-wavenumber analyses have been employed numerous times to improve data quality and understanding, primarily as applied to guided waves. Ruzzene applied frequency-wavenumber filtering to improve damage visualization by isolating defect-scattered waves in the LDV-imaged wavefield [32]. Tian and Yu utilized multidimensional Fourier domain transformations to decompose multi-modal Lamb waves into their constituent modes and apply digital filtering for defect detection and characterization [33]. Material defects such as disbonding in multilayered isotropic materials and delaminations in anisotropic materials pose interesting challenges to typical ultrasonic NDE scattering analyses because bulk and guided wave scattering may be largely dependent on the geometry of the defect. Although an incident guided wave may scatter some from the discontinuity introduced by the disbond or delamination, the wavenumber may also shift over the delamination due to dispersion. Consequently, it may be easier to detect wavenumber shifting as opposed to scattering. In such cases, a Fourier transformation of the wavefield data can illuminate

any significant wavenumber shifts. Sohn *et al.* analyzed guided wavenumber patterns to develop detection algorithms for automatically detecting delaminations and disbonds in LDV-imaged wavefields [34]. Filtering techniques have also been developed to separate guided wave modes [31, 33] and bulk wave modes [35, 36], so each mode can be analyzed independently in either Fourier or time-space domains.

2.4 Research Objectives

The primary objective of this work is to quantify scattering of angle-beam shear waves from a scatterer of interest (SOI) that is part of a compound scatterer in bonded isotropic metallic plates. Working towards this objective has also resulted in improved methods for acquiring wavefield image data, acquisition of wavefield image data from relevant and unique specimens, and development of wavefield analysis techniques. Most previous work on buried notch interrogation using angle-beam inspection has consisted of modeling and theoretical behavior analyses. Moreover, experimental wavefield data on buried notches emanating from fastener holes in layered media are lacking in the UT community. Access to such data could provide invaluable information for model validation and help push forward current research on buried defect detection in layered homogeneous isotropic plates that are commonly used in the aerospace industry. This thesis aims to provide data acquisition methods and analyses for wavefield imaging data relevant to the aerospace industry.

Acquired wavefield data for three unique bonded specimens are presented. Experimental parameters and their effects on acquired data quality are discussed in detail, and bonded specimen design and fabrication is explained. Wavefield baseline subtraction is examined and compared to other wavefield analysis techniques used to present and quantify relevant scattering data. Finally, experimental results are presented to demonstrate the utility of discussed techniques to quantify angle-beam shear wave scattering from compound scatterers.

CHAPTER 3
EXPERIMENTAL PROCEDURES

This chapter describes the experimental setup and procedures used to acquire angle-beam wavefield data, details bonded specimen design criteria and fabrication techniques, and summarizes the experiments performed to acquire the wavefield data used throughout this research.

3.1 Experimental Setup

The experimental setup consisted of a scanning LDV system, ultrasonic transducers mounted atop of fabricated bonded specimens, and pulse signal excitation equipment to excite and acquire local wavefield data around a compound scatterer. Two types of scans were acquired: line scans (presented as B-scans) and area scans (presented as both B-scans and C-scans).

3.1.1 Acquisition Method

Bulk wave inspection was conducted using broadband transducers with a center frequency of 5 MHz, and data were acquired using a laser Doppler vibrometer (LDV) mounted on a XYZ translation stage. LDV scans were taken on a point-by-point basis, and the excitation signal was a negative impulse (spike) with a slow decay. LDV measurements are very sensitive to both temporal and spatial variations at these frequencies, so temporal and spatial Nyquist rates were carefully considered. Furthermore, preparation of the scanning surface and signal averaging were utilized to reduce temporal and spatial noise. Figure 3.1 displays the signal flow for the experiments in a modified block diagram form.

3.1.2 Sampling Considerations

Wavefield measurements sample the propagating waves in both time and space, so both temporal and spatial sampling intervals must be considered. Temporal sampling is determined by the Nyqiust frequency, which is twice the maximum frequency present in the signals of interest. The sampling period, Δt, must meet the following condition:

$$\Delta t < \frac{1}{2f_{\max}}. \tag{3.1}$$

Similar to temporal sampling, the spatial sampling interval must meet the following condition,

$$\Delta x < \frac{\lambda_{\min}}{2}, \tag{3.2}$$

$$\lambda_{\min} = \frac{c_{\min}}{f_{\max}}, \tag{3.3}$$

where $\lambda_{\min}$ is the minimum wavelength, $c_{\min}$ is the minimum wave speed, and $f_{\max}$ is the maximum frequency. The signal to be sampled is low-pass filtered at 10 MHz, so the minimal temporal sampling frequency must be 20 MHz (i.e., the Nyquist rate) to avoid aliasing. However, since the digitizer clock is not synchronized with the excitation signal, a sampling frequency of 100 MHz is used to minimize jitter. The slowest propagating wave mode is the surface-bound Rayleigh wave. Assuming the nominal Rayleigh wave velocity is 2.90 mm/μs and the highest frequency is 10 MHz, Eq. 3.2 yields a minimum sampling interval of 0.15 mm. It has been shown that spatial sampling, not temporal, is the limiting factor for excessive scan times [28, 37]. A spatial sampling interval of 0.15 mm yields scan times upwards of 5 hours, so larger spatial sampling intervals (i.e., 0.25 mm) were used to reduce scan times at the expense of some spatial aliasing, primarily of the Rayleigh waves.

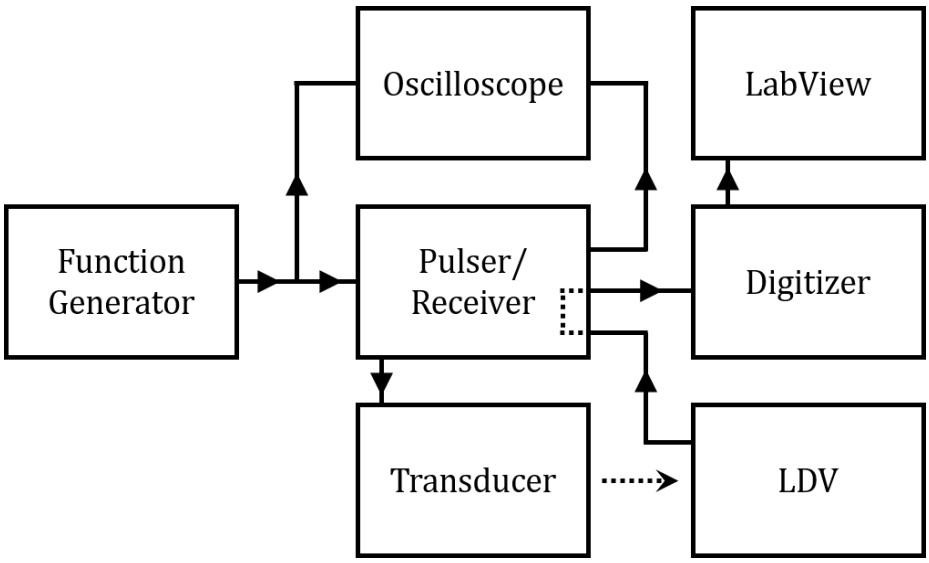

Figure 3.1: Block diagram of experimental setup

3.1.3 Data Acquisition

It is important to note that LDV-measured data contain much more low-frequency information than a typical pulse-echo or pitch-catch measurement because the LDV is a broadband receiver whereas piezoelectric receivers naturally have a higher Q. In pulse-echo or pitch-catch, the use of angle-beam shear wedges forces transmitted and received energy to be incident beyond the first critical angle, which allows for natural mode filtering: compressive waves are converted to Rayleigh waves (SAWs), and primarily shear energy is transmitted into the bulk material. In order to remove some of the unwanted lower frequency information from LDV-measured data, the raw signal from the LDV is band-pass filtered using a Panametrics 5072PR Pulser-Receiver from 1-10 MHz as shown in the block diagram in Figure 3.1; this filter also removes unwanted high frequency noise. For this work, 5 MHz was the frequency for inspection, so information in the upper frequency range of the measured signal (i.e., $>$ 8 MHz) is less significant. Furthermore, post-acquisition frequency-wavenumber processing was typically band-limited to about 6 MHz to avoid spatial aliasing. Figure 3.2 illustrates the spectral distribution for a line scan of a 6.35 mm-thick 6061 aluminum plate with a 6.35 mm diameter through-hole. Figures 3.2(b) and

3.2(d) show that measured signal energy is skewed towards the lower frequencies due to the broadband LDV receiver.

Signal averaging was used to improve the SNR. It was determined through trial and error that 128 averages yielded a reasonable balance between data quality and scan time. Previous work made use of chirp signals and deconvolution to acquire a range of tone-burst equivalent response signals with each scan [28, 38]. Here, a broadband impulsive excitation (spike) was generated using a 5072PR Panametrics pulser-receiver triggered by a 1 kHz signal generated from an Agilent 33250A function generator. Prior work has shown that the spike excitations are equivalent to chirp excitations following deconvolution to an impulse [37].

All relevant data in this thesis were acquired using an angle-beam ultrasonic probe consisting of a Panametrics ABWM-4T 60° angle-beam acrylic wedge and one of two 5 MHz Olympus transducers: transducer A (Model # C543-SM, SN 867921) and transducer B (Model # C543-SM, SN 1007263). The frequency response of both transducers was tested by analyzing a back-wall echo from a pulse-echo measurement. A summary of all equipment used to acquire data is included in Appendix A.

3.2 Specimen Design

A two-layer bonded specimen including fastener holes and simulated defects was designed, fabricated and used for the work presented in this thesis. Three versions of the bonded specimen were created to investigate scattering from various notch geometries and orientations. Each specimen was sufficiently large compared to the scan area so that edge reflections could be neglected, and the scanning surface was mirror-finished to maximize the signal-to-noise ratio for the recorded LDV signals. This section details the design logic and fabrication considerations for the first bonded specimen design as well as the subsequent two specimens that were made to address a range of defect conditions.

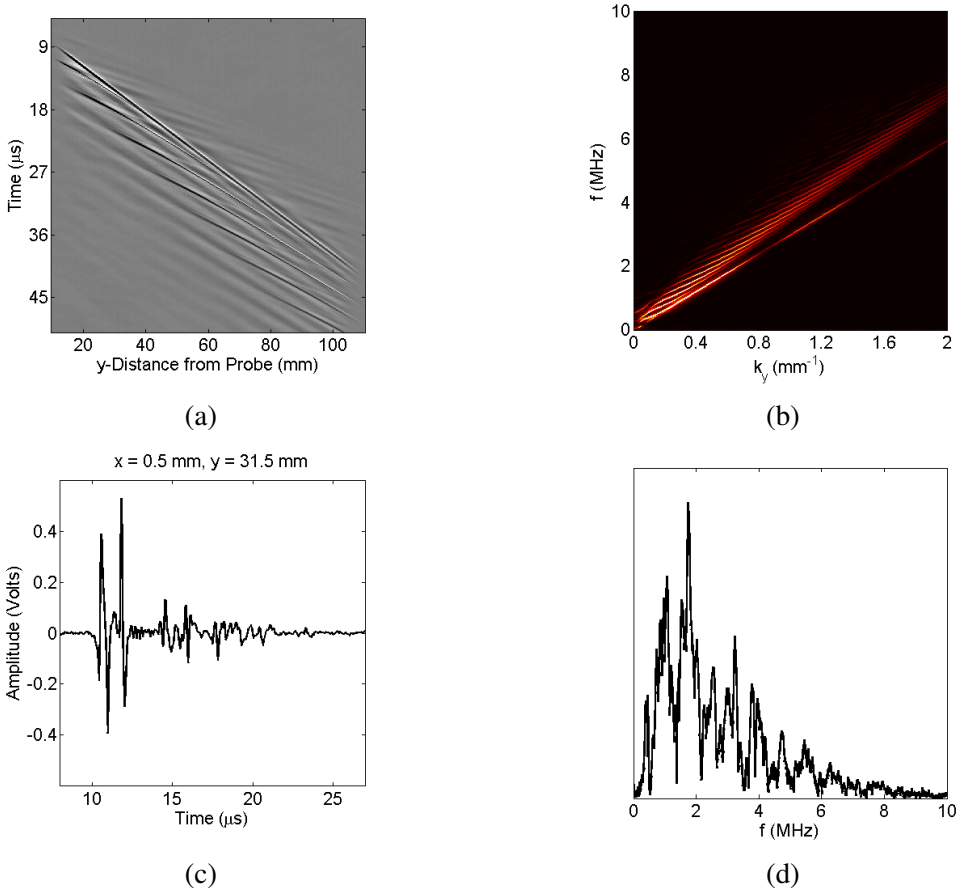

Figure 3.2: (a) B-scan of measured data, and (b) its Fourier domain representation. (c) A-scan of signal measured at $y = 14$ mm in the B-scan and (d) its spectrum

3.2.1 Design Parameters

Several design parameters were defined for the bonded specimen to create a relatively controlled scattering environment in the bulk of the specimen and to acquire high quality data efficiently. Results and data from previous single-layer specimens, such as those in [39, 37], were used as benchmarks for determining the relative quality of acquired data. The specimen design criteria are as follows:

- Multi-layered, isotropic material relevant to aerospace industry
- Multiple fastener holes (through-holes)
- Controlled, buried defects emanating from fastener holes (known geometry and ori-

entation)

- Test and compare two notch (crack-like defect) designs
- Ensure maximum incident energy strikes the notch

6061 aluminum was chosen as the isotropic material for this work because its material properties are very similar to the properties of aerospace-grade aluminum. Each specimen contained three 6.35 mm diameter through-holes that were drilled for slip fit tolerances (i.e., 6.4008 ± 0.0127 mm). Both a hand-cut corner notch and electronic discharge machined (EDM) notches with quarter-circular profiles were considered. The notches were also inspected in two different orientations relative to the direction of the beam path: 45° and 90°. Figures 3.4(c) and 3.5(c) illustrate the two notch designs and orientations.

Bonded specimens present unique challenges for quantifying scattering because of the additional complexity of the interface interactions. One particular challenge is the reduction of scattered energy. Since the bottom layer has the same material properties as the top layer (i.e., acoustic impedance, density, anisotropy, etc.), more wave energy will transmit into the bottom layer rather than reflect back into the top layer as compared to a single layer plate. This can reduce the SNR because the wavefield is measured on the top surface. To help ensure that maximum incident energy interacts with the defect, the bottom layer is bisected so that both interface interactions during the first full skip occur at aluminum-air interfaces. Figure 3.3 illustrates the effect of energy leakage in the bonded specimen by comparing radial energy plots (described in section 5.2) for both single layer and bonded specimens. The aim point for interrogation was along the right tangent of the through-hole at an approach angle of -90° relative to the positive x-axis. No notch was present in the data shown in Figure 3.3. Signal excitation and data acquisition were identical whereas the specimen itself was the only variable in the experiment for Figure 3.3. Although energy loss is visible in the bonded specimen plot, the specimen design helps contain the majority of the incident energy inside the top layer for stronger defect scattering SNR from the LDV.

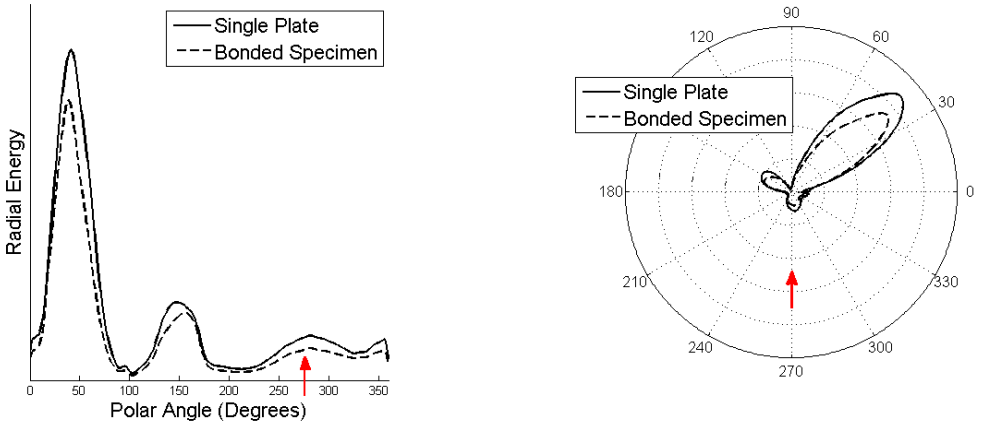

(a) (b)

Figure 3.3: Radial energy of single plate and bonded (two-layer) plate specimens in (a) rectangular and (b) polar plots

3.2.2 Specimen Fabrication

The first iteration of the bonded specimen specimen was fabricated from two mirror-finished aluminum 6061 plates bonded together using degassed EA E-120HP Loctite epoxy. The bonded specimen dimensions were 280 mm $\times$ 280 mm $\times$ 9.53 mm with three holes of 6.35 mm diameter drilled into the specimen: two undamaged through-holes and one with a 3 mm-long, 45° corner notch emanating from a through-hole on the far-surface of the "top" (i.e., the scanning surface) plate. Figure 3.4(a) shows sketches of the top view of the plate.

As shown in the side view of the specimen via Figure 3.4(c), angle-beam shear waves were generated using one of the two 5 MHz, 6.35 mm diameter Olympus transducers attached to an acrylic wedge as discussed previously. Wavefield sensing was conducted using a Polytec LDV mounted on an XYZ scanner. As shown in Figure 3.4(c), the transducer was placed 1.5 skips (three path lengths) away from the notch-through-hole intersection. The equivalent surface distance (shown in Figure 3.4(c)) was found using the geometric relation

of the material thickness and angle of incidence,

$$d = 3h \times \tan(\theta_r), \tag{3.4}$$

where $d = 29.1$ mm is the surface distance from beam incidence to the SOI, $h = 6.35$ mm is the thickness of the top plate, and $\theta_r = 56.8^\circ$ is the angle of refraction in 6061 aluminum. For most acquired data, it was found that aiming the probe at the connection point of the notch and through-hole yielded the best scattering from the SOI (i.e., the notch). It is important to note that the probe location was calculated according to the nominal refracted angle, $\theta_r = 56.8^\circ$, which assumes that the ultrasonic transducer emits a beam-like wavefield (i.e., a coherent beam). A discussion of the technical details of ultrasonic beam propagation and its effect on scattering analysis is included in Chapter 5.

The two 6061 aluminum plates comprising the bonded specimen were riveted together, and three 6.35 mm through-holes were drilled along a line located 165 mm from one edge of the plates. The "bottom" 3.175 mm plate was bisected at 127 mm from the same reference edge, ensuring that 12.7 mm of the bottom plate was accessible to propagating bulk waves before the through-hole. The bottom plate bisection was done to ensure that the first skip occurred at the aluminum-air boundary to minimize energy leakage into the bottom layer. This is important for ensuring that the majority of shear wave energy interacts with the buried notch at the far-surface of the top plate.

The second bonded specimen contained three through-holes with electrical discharge machined (EDM) notches emanating from two of the three through-holes. Both 2 mm and 4 mm quarter-circular back-surface notches were machined. Otherwise, the material and construction of the second specimen was identical to that of the first. The specimen contained one undamaged through-hole, one with a 4 mm-long, EDM notch emanating from the through-hole at -45° orientation, and one with a similar 2 mm-long notch oriented at -45° in the x-y plane as depicted in the top view of Figure 3.5.

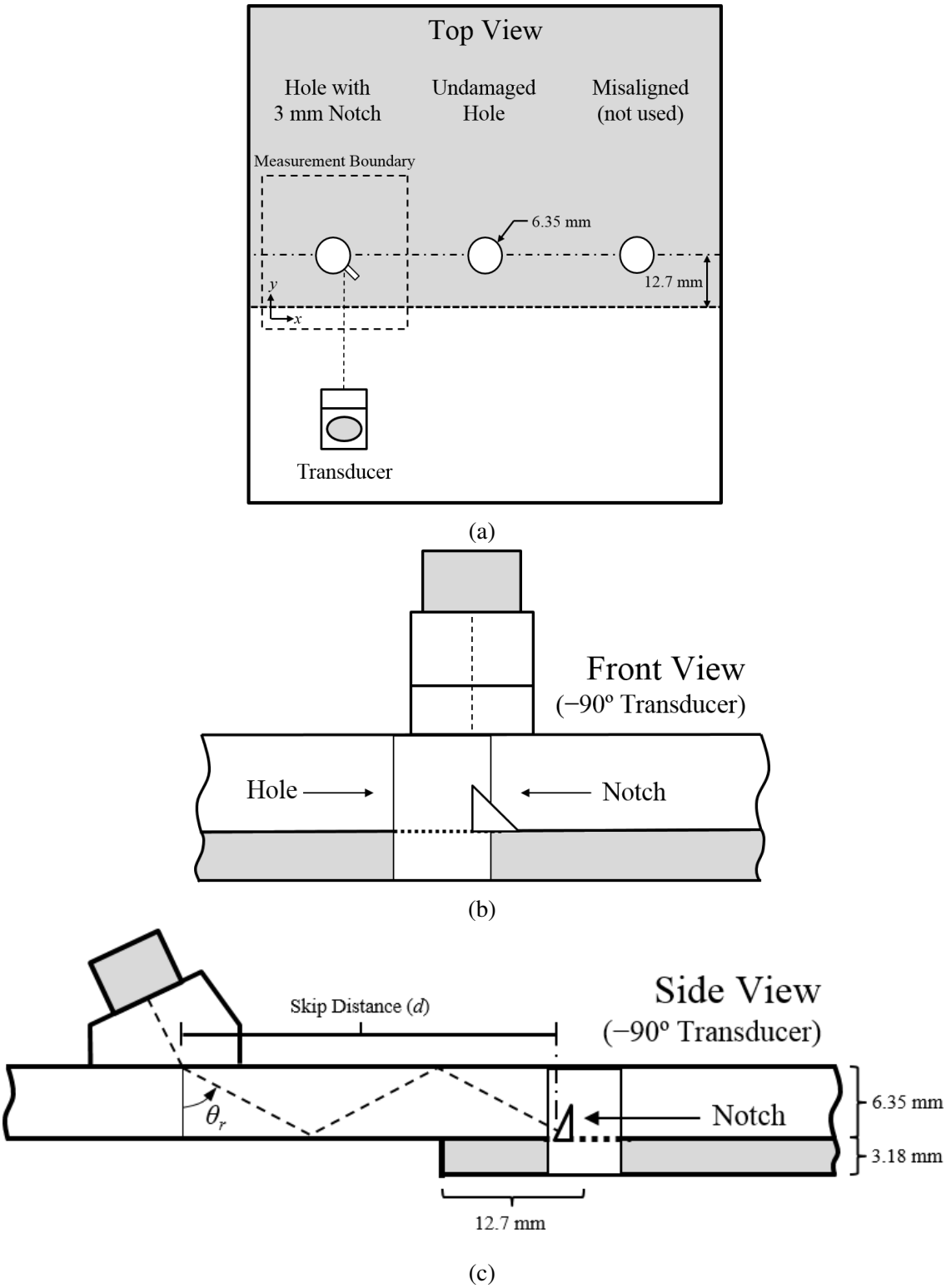

Figure 3.4: (a) Top view of bonded specimen #1 showing measurement area, (b) front view with non-skewed notch geometry, and (c) side view with beam path

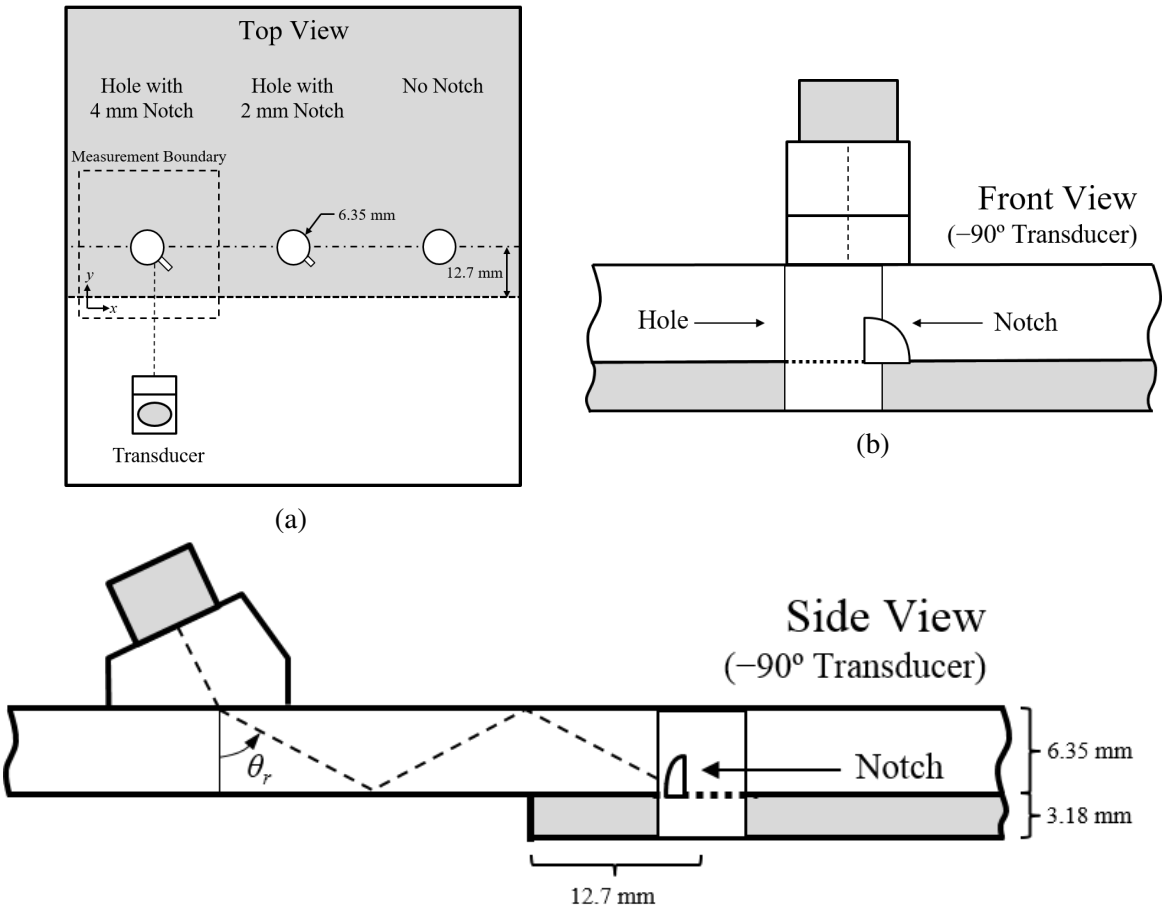

Figure 3.5: (a) Top view of bonded specimen #2 showing measurement area, (b) front view with non-skewed notch geometry, and (c) side view with beam path

The three through-holes were drilled through the two-layer plate with the notches machine-cut on the far side of the upper plate prior to bonding. Front and side views of the specimen are also shown in Figure 3.5, and the side view shows where the edge of the lower plate falls relative to the path of the nominal skip. Similar to the first specimen, it was designed such that the first reflection of the incident waves from the bottom of the first plate (i.e., the first half-skip) occurs well before this edge to prevent energy leakage into the lower plate. A typical angle-beam inspection would operate at the half-skip distance rather than the 1.5 skip distance, but that was not possible here since the probe would partially block the scan area. For the unbonded specimens, this difference is not critical since there is

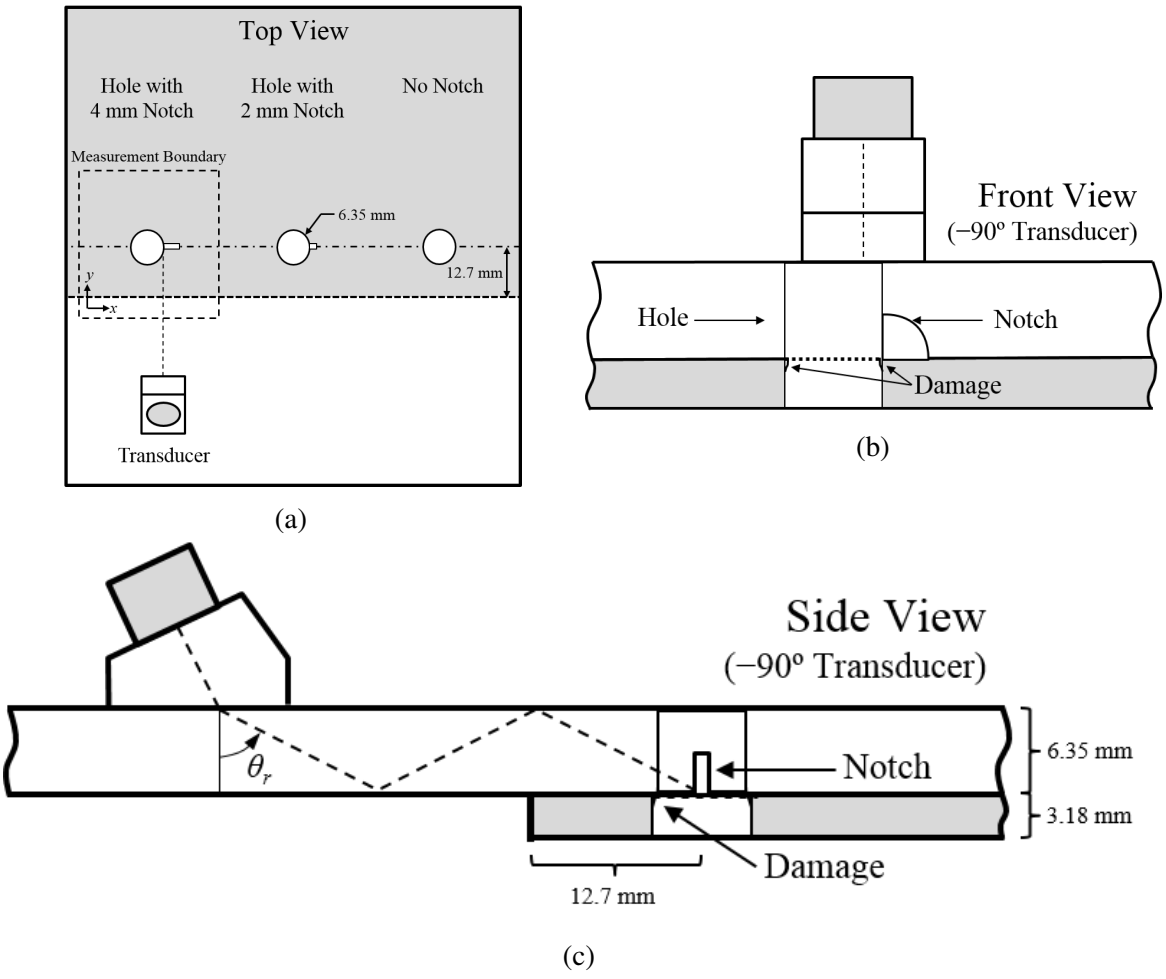

Figure 3.6: (a) Top view of bonded specimen #3 showing measurement area, (b) front view with non-skewed notch geometry, and (c) side view with beam path

minimal energy leakage at the aluminum-air interface. However, for the bonded specimen, the possibility for energy leakage into the lower plate was reduced by cutting back its size.

The third and final bonded specimen, shown in Figure 3.6, was designed to consider the effect of broadside incidence to the notch. The third specimen design was altered from the previous two designs to contain 2 mm and 4 mm EDM notches oriented at $0°$. Otherwise, the specimen was designed and fabricated to the same specifications as the second one. It is important to note that bonded specimen #3 contained abrasions on the inside surface of the notched through-holes due to a fabrication error. The specimen was not re-fabricated given project time constraints, so wavefield data from this specimen contain additional through-

hole scattering. Although notch scattering quantification in the presence of other scattering due to surface abrasions was not the focus of this work, it is reasonable to use a specimen with such characteristics because they are relatively common in the aerospace industry.

Challenges and Precision/Repeatability Limitations

The high-frequency (i.e., small wavelength) nature of data acquisition in this thesis posed several interesting challenges during specimen fabrication. Because the average bulk wave wavelength was on the order of 0.5 mm, small alterations in machining led to significant effects in the measured wavefield. For example, a common technique for locating a hole center for alignment purposes is to re-drill the drilled through-hole with the same size drill bit on a mill. However, doing this procedure with drill-bits that are not normal to the drilling surface can create slightly wider drill marks in the bulk of the plate along the inner surface of the through-hole. It was found that bonded specimen #3 bore these imperfections and consequently the acquired data showed double scattering from the through-holes.

Scans of the same measurement area proved to be highly repeatable even with global repositioning of the specimen. However, scans from different through-holes with the same experimental parameters did not match up as well, likely due to variations in machining and probe location relative to the SOI. Unintentional probe displacement was found to be the most significant factor in producing non-repeatable scans of the same measurement area. Precision limits were estimated to be 0.4 mm based on the measuring tools available in the lab.

3.3 Summary of Experiments

3.3.1 Line Scans

Preliminary wavefield measurements were performed as line scans prior to area scans because the scan time is an order of magnitude lower for line scans. Furthermore, line scans provide a rapid display of B-scans that are used to affirm beam skip behavior and probe

alignment. Figure 3.7 shows the comparison of scans L1-L4, which are listed in Table 3.1. Red lines (in B-scans) and red circles (in C-scans) indicate the through-hole boundary. Although through-hole noise measured during the scans was not windowed for the B-scans shown in Figure 3.7, noise caused by the through-hole was suppressed using a radial Tukey window for all other data and results presented in this work. Recall that both transducer A (Model # C543, SN 867921) and transducer B (Model # C543-SM, SN 1007263) have 5 MHz center-frequencies and perform similarly. Only a few line scans were performed on the top plate of the third bonded specimen prior to bonding because of their limited utility for scattering analysis. Table 3.1 summarizes the various line scans acquired throughout this thesis.

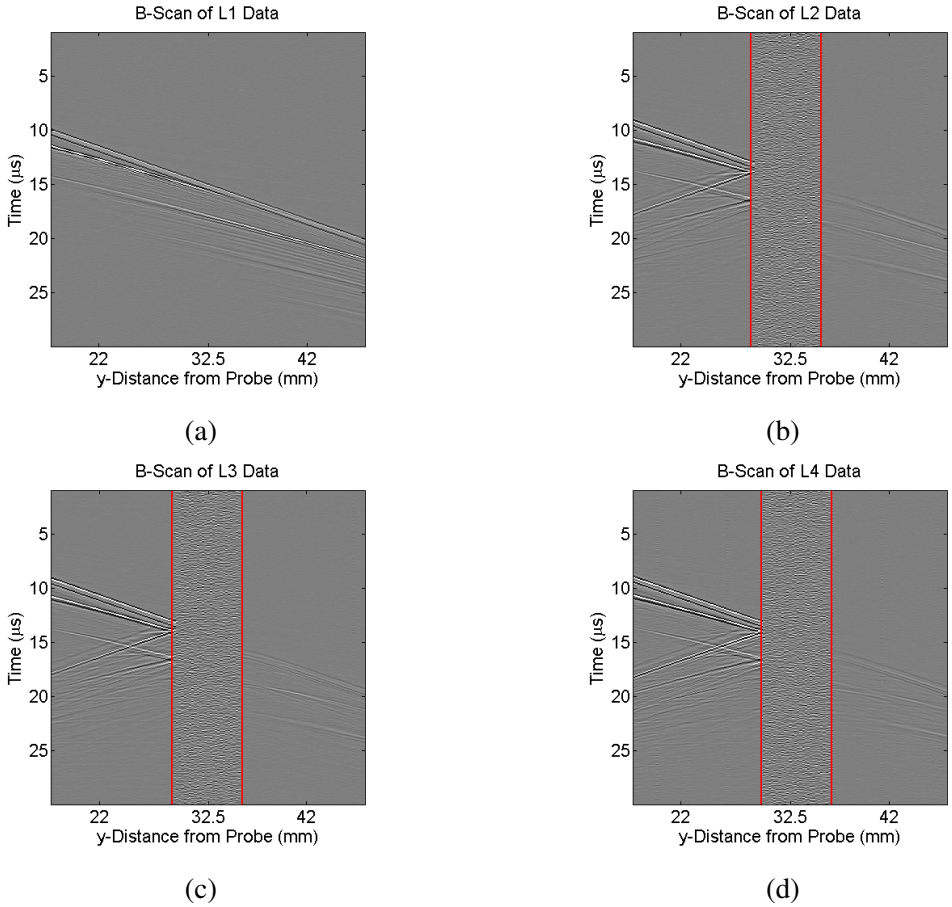

Figure 3.7: B-Scans showing line scan data for (a) plate with no scattering features, (b) 6.35 mm diameter through-hole, (c) 6.35 mm through-hole with 2 mm EDM notch, and (d) 6.35 mm through-hole with 4 mm EDM notch

Table 3.1: Summary of line scans.

Scan Number	Transducer	Description	Specimen
L1	B	No damage	Single Plate
L2	B	Through-hole with no damage	Single Plate
L3	B	Through-hole with 2 mm EDM notch	Single Plate
L4	B	Through-hole with 4 mm EDM notch	Single Plate

3.3.2 Area Scans

Area scans were the primary form of acquisition for this thesis and are summarized in Table 3.2. All scans reported here were conducted over a 30 $\times$ 30 mm area. As mentioned before, the spatial sampling rate is the limiting factor for determining scan run-time. Therefore, a consistent sampling rate was used once it was determined that 0.25 mm/pixel yielded the best trade-off between scan run-time and data quality. It is important to note that area scans B3-B5 were performed with the probe aimed near the through-hole apex (i.e., the aim point was determined empirically using pulse-echo scans) whereas all other area scans had the probe aimed at the calculated through-hole and notch connection point (e.g., $+3.18$ mm offset from the hole apex for bonded specimen #3). Table 3.3 summarizes the nominal aim points and measured probe locations, which are given based on the location of beam incidence referenced from the center of the through-hole. The probe was to be placed so that beam incidence was 1.5 skips (i.e., a surface distance of 29.11 mm) from the nominal aim point for each scan, but there were small displacements in measured probe location due to precision limitations. Although scans B1-B2 and B6-B8 are aimed at the notch-through-hole intersection, they do not share the same physical aim point because the notch is oriented at -45° for bonded specimen #1 and at 0° for bonded specimen #3.

Table 3.2: Summary of area scans.

Scan Number	Transducer	Description	Specimen
A1	B	Through-hole with no damage	Single Plate
A2	B	Through-hole with 2 mm EDM notch	Single Plate
A3	B	Through-hole with 4 mm EDM notch	Single Plate
B1	A	Through-hole with no damage	Bonded #1
B2	A	Through-hole with 2 mm corner notch	Bonded #1
B3	A	Through-hole with no damage	Bonded #2
B4	A	Through-hole with 2 mm EDM notch	Bonded #2
B5	A	Through-hole with 4 mm EDM notch	Bonded #2
B6	B	Through-hole with no damage	Bonded #3
B7	B	Through-hole with 2 mm EDM notch	Bonded #3
B8	B	Through-hole with 4 mm EDM notch	Bonded #3

Table 3.3: Summary of probe aim point and location details.

Scan Number	Probe Location (mm)	Aim Point
A1	$(3.38, -29.51)$	Notch-Through-hole Intersection
A2	$(3.18, -29.41)$	Notch-Through-hole Intersection
A3	$(3.08, -29.01)$	Notch-Through-hole Intersection
B1	$(2.25, -30.84)$	Notch-Through-hole Intersection
B2	$(2.25, -31.64)$	Notch-Through-hole Intersection
B3	$(1.2, -31.11)$	Hole Apex $+1.5$ mm in x
B4	$(1.3, -32.01)$	Hole Apex $+1.5$ mm in x
B5	$(1.5, -31.91)$	Hole Apex $+1.5$ mm in x
B6	$(3.18, -29.21)$	Notch-Through-hole Intersection
B7	$(3.28, -29.21)$	Notch-Through-hole Intersection
B8	$(3.18, -27.61)$	Notch-Through-hole Intersection

CHAPTER 4
FREQUENCY-WAVENUMBER ANALYSIS

Frequency-wavenumber analysis refers to the use of processing and filtering algorithms implemented in either the 2-D (ω, k) or 3-D (ω, k_x, k_y) Fourier domains. Analysis techniques used for separating wave modes and segregating an SOI from full wavefield data are discussed. Furthermore, applications to various types of wavefield scans acquired from three versions of bonded specimens are shown.

4.1 Wavefield Data Pre-processing

Acquired wavefield data are typically in need of some pre-processing to prepare it for further frequency-wavenumber processing and analyses. 20% Tukey windows are applied spatially and temporally to raw wavefield data to minimize spectral leakage in the Fourier domain. As discussed in section 3.1.3, LDV-acquired data contain a significant amount of low frequency information because the LDV is a broadband receiver. Post-acquisition processing, such as digital filtering, can be used to remove noisy low frequency components that may otherwise be skewing scattering responses in the wavefield. One such technique used was to convolve the data with a 5 MHz, 2 cycle tone burst. Figure 4.1 shows the effect of applying a 5 MHz, 2 cycle tone burst to broadband wavefield data excited by a 5 MHz center frequency PZT and acquired using an LDV system. Comparing Figures 4.1(b) and 4.1(c), it appears as though the SNR has reduced and spectral smearing has occured. In fact, the mid-frequency components are now the strongest in the spectrum due to the convolution process, so the change in color scale reveals a more accurate SNR of the frequencies of interest. Figure 4.1(g) shows the reduction of low frequency components at a specific point in the wavefield. Table 4.1 summarizes the pre-filtering used for all wavefied data. Wavefield data with different pre-processing were not compared directly to

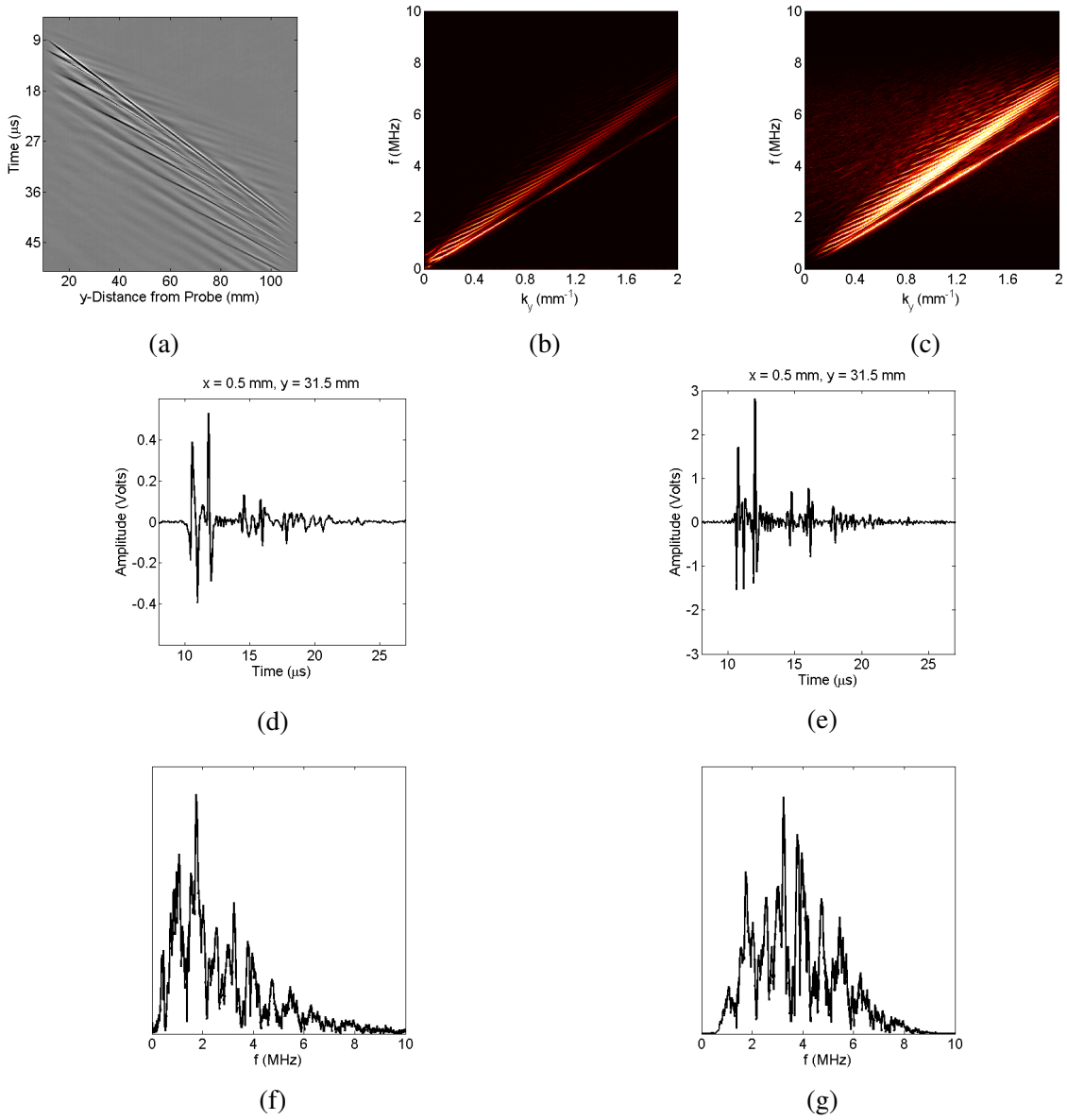

Figure 4.1: (a) B-scan of measured data A1, and the frequency-wavenumber representation of (b) unfiltered and (c) filtered signals. A-scan of (d) unfiltered signal measured at a specified location and (e) filtered signal with (f) its unfiltered and (g) filtered spectra

each other in subsequent analyses.

4.2 Phase Velocity as Measured on the Surface

As mentioned previously, there are three primary wave modes present in the experimental data: Rayleigh, shear and longitudinal. Each wave mode propagates at different phase

Table 4.1: Summary of wavefield pre-filtering.

Scan Number	Tone Burst
A1	5 MHz, 2 cycle
A2	5 MHz, 2 cycle
A3	5 MHz, 2 cycle
B1	No Convolution
B2	No Convolution
B3	5 MHz, 2 cycle
B4	5 MHz, 2 cycle
B5	5 MHz, 2 cycle
B6	5 MHz, 2 cycle
B7	5 MHz, 2 cycle
B8	5 MHz, 2 cycle

velocities where the nominal phase velocities are assumed to be 2.9 mm/μs for the Rayleigh mode and 3.1 mm/μs and 6.3 mm/μs for the shear and longitudinal modes, respectively. Because the Rayleigh mode is bound to the plate surface, its measured phase velocity is very similar to its wave speed. However, since shear and longitudinal modes propagate in the bulk of the material and acquired data is measured on the surface of the plate, the measured phase velocity becomes a function of the angle of refraction of each propagating wave. In fact, this projection can be accounted for by implementing a simple geometric transformation to the wave speed, c,

$$c_p = \frac{c}{\sin(\theta_r)}, \tag{4.1}$$

where c_p is the measured phase velocity. Shear waves at a small refracted angle can thus be confused with longitudinal waves at larger refracted angles.

The phase velocity of surface-measured bulk waves can also be skewed if measured along a line at a non-zero angle to the propagation direction as shown in Figure 4.2. The skew angle, α, expands the apparent wavelength by a factor of $1/\cos(\alpha)$, increasing the measured phase velocity. When combined with the refracted angle correction from before,

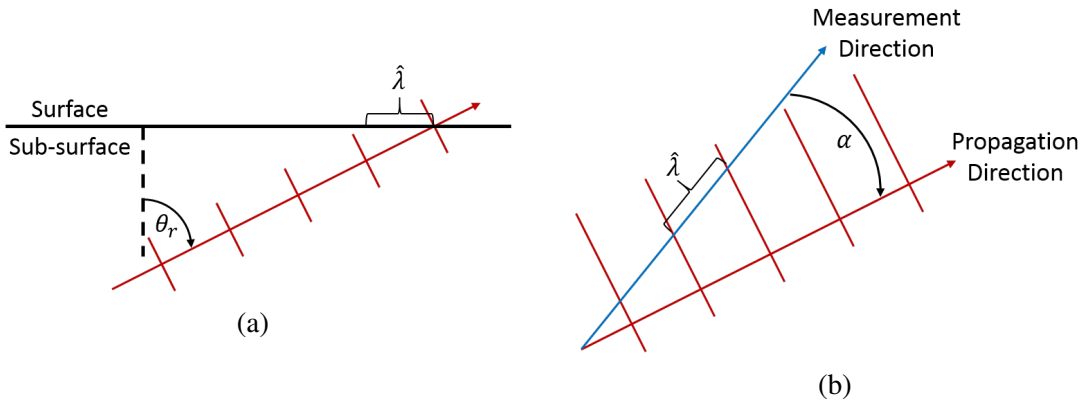

Figure 4.2: Phase velocity measured (a) at the surface and (b) along skewed angle

the measured phase velocity is

$$c_p = \frac{c}{\sin(\theta_r)\cos(\alpha)} \tag{4.2}$$

Data acquisition was performed so that the skew angle resulting from line scans was minimized (i.e., the probe was carefully positioned to minimize deviation from its -90° position relative to the positive x-axis).

The ambiguity between wave modes is evident in the Fourier domain, where k_x-k_y slices can be used to determine the range of phase velocities for each mode. Consequently shear and longitudinal wave mode ambiguity exists and complicates the determination of such phase velocity boundaries. Section 4.5 presents a series of phase velocity filters used to filter each mode from the measured wavefield.

4.3 Line Scan Processing (2-D FFT)

The 2-D FFT can be applied to a B-scan generated from either a line scan or a slice of an area scan. As mentioned earlier, B-scans are a function of time and one spatial dimension, so their FFT represents the frequency and one-dimensional wavenumber of the data. Figure 4.1(a) illustrates time-windowed B-scan data produced from scan L1, and Figures 4.1(b) and 4.1(c) show its frequency-wavenumber representation before and after time domain

filtering. The post-filtered spectrum is re-centered so that low frequency components no longer dominate the spectral content of the measured signals. Furthermore, the distinction between Rayleigh and shear waves can be made clearly in the frequency-wavenumber domain in Figure 4.1(c). Recall that the measured phase velocity, here given as $c_p = \omega/k_r$, for shear waves is greater and covers a larger range than that of Rayleigh waves due to the larger range of refracted angles at which shear waves can be emitted into the bulk. Shear wave amplitude can thus be seen in Figure 4.1(c) as the broader, steeper slope whereas Rayleigh wave amplitude is the more well-defined shallower slope. Little to no longitudinal wave amplitude is visible in this plot due to the fact that waves were incident past the first critical angle.

Radial line scans can also be generated from C-scan data. 3-D Cartesian data (t, x, y) are transformed into polar coordinates (t, r, θ) by radially interpolating area scan data from the through-hole edge (4 mm from the center of the through-hole) to a radial length of 13 mm (near the scan area boundary) as shown in Figure 4.3(a). After the radial interpolation, data are represented as angle-dependent radial line scans. Just as before, each line scan is represented as a B-scan and is a function of time and distance, which now corresponds to the radial distance. Figure 4.3(b), 4.3(c), and 4.3(d) show B-scans for radial lines at 90° (relative to the positive x-axis), 270° (or -90° relative to the positive x-axis) and 15°, respectively. The radial path lengths for each line scan were chosen to avoid noise from the through-hole. Each time-radius slice is converted into the frequency-wavenumber domain (ω-k_r) via the 2-D FFT and is shown in Figures 4.3(e), 4.3(f), and 4.3(g). Radially outward propagating (moving in the $+r$ direction) waves have positive radial wavenumber, $+k_r$, and are represented in the first quadrant $(+\omega, +k_r)$. Radially inward propagating waves (r) are in the second quadrant $(+\omega, -k_r)$, and the third and fourth quadrants are mirror images of the first two.

The 90° slice shows incident and scattered waves in the $+r$ direction as both are outward-propagating from the hole. Corresponding Fourier data are located in the first

and third quadrants. The 270° slice shows both incident and backscattered waves in the $\pm r$ directions as shown in Figure 4.3(c). Since incident waves are inward-propagating $(-r)$ relative to the hole, they appear in the second and fourth quadrants while the backscattered waves are visible in the first and third quadrants in Figure 4.3(f). Because the radial lines for both the 90° and 270° cases correspond to the propagation directions, the only phase velocity ambiguity is due to the refracted angle.

Figure 4.3(d) shows a time-radial slice at 15°, which does not correspond to either forward or backward propagating waves. Because the polar angle is skewed from the propagation direction by 75°, the apparent phase velocities should increase by a factor of $1/\cos(75^\circ)$, or 3.86. This effect can be seen in the frequency-wavenumber plot of Figure 4.3(g) where the stronger incident wave energy has been shifted to a steeper angle corresponding to higher phase velocities when compared to Figure 4.3(e). However, scattered shear and Rayleigh waves, which are propagating close to the 15° line, do appear near their nominal phase velocities.

4.4 Area Scan Processing (3-D FFT)

The processing applied to area scans is similar to the processing applied to line scans. The 3-D Fourier transform is used to transform full 3-D wavefield data from the time-space domain (t, x, y) to the frequency-wavenumber domain (ω, k_x, k_y). Area scan A1 is used as an example of applying a 3-D FFT to C-scan data. The 3-D frequency-wavenumber domain of C-scan data is conical shaped due to the increase of wavenumber with increasing frequency. Figure 4.4(a) shows a snapshot of A1 at 15 μs and a slice of its 3-D FFT at 5 MHz is shown in Figure 4.4(b).

4.5 Phase Velocity Filtering

The objective of phase velocity filtering is to separate Rayleigh, shear, and longitudinal waves by their respective phase velocity ranges as summarized in Table 4.2. The wave-

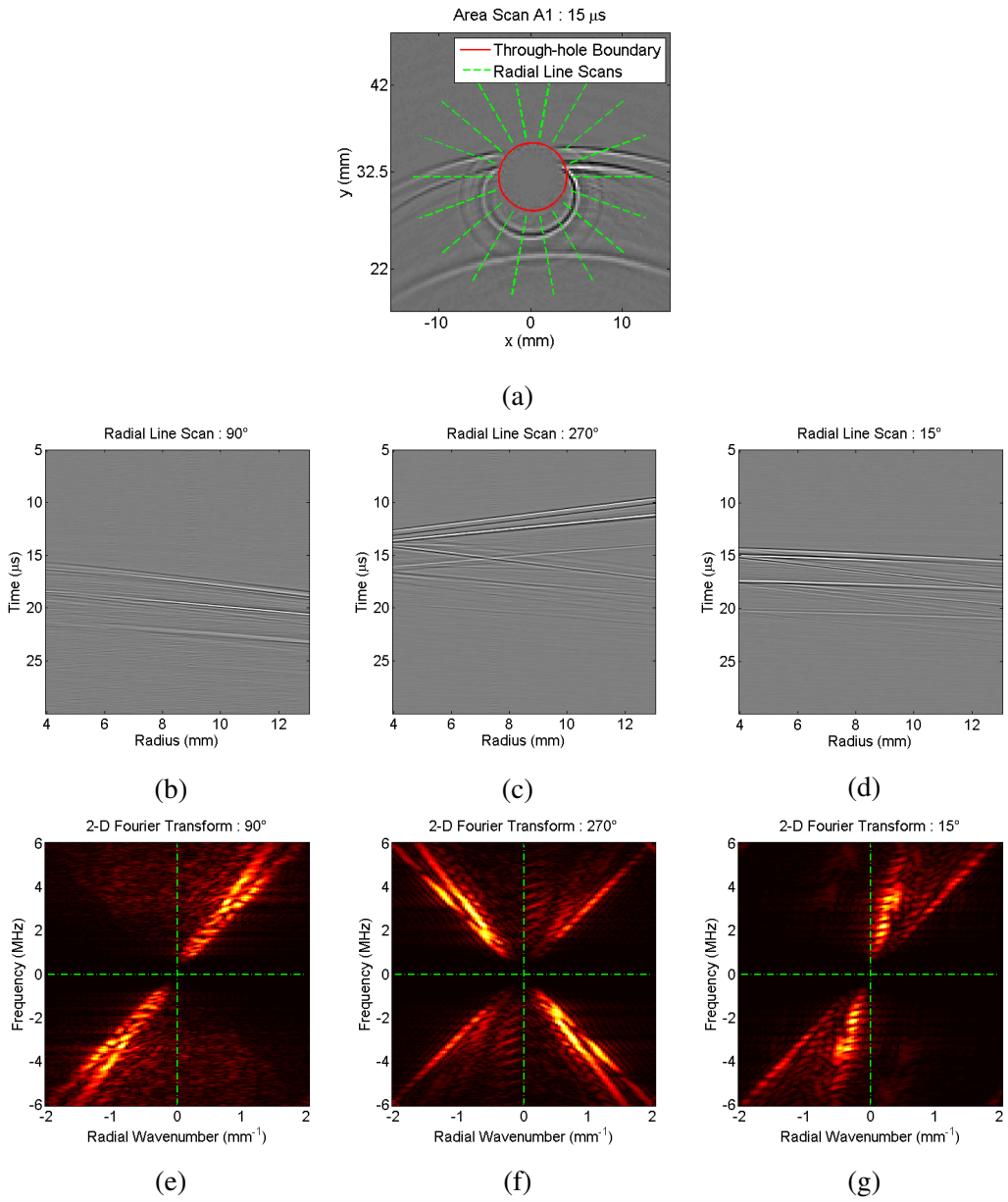

Figure 4.3: Radial line scans processed from scan A1 and their 2-D frequency-wavenumber representations

field is transformed to the frequency-wavenumber domain via a 3-D FFT. Ring filters are designed and applied to the 2-D wavenumber space across all relevant frequencies. Figure 4.5 illustrates the process using scan A1 at 5 MHz; the phase velocity boundaries are marked with green circles. Figure 4.5(a) shows the data in the frequency-wavenumber domain. Concentric rings mark the collection of wave energy corresponding to the phase

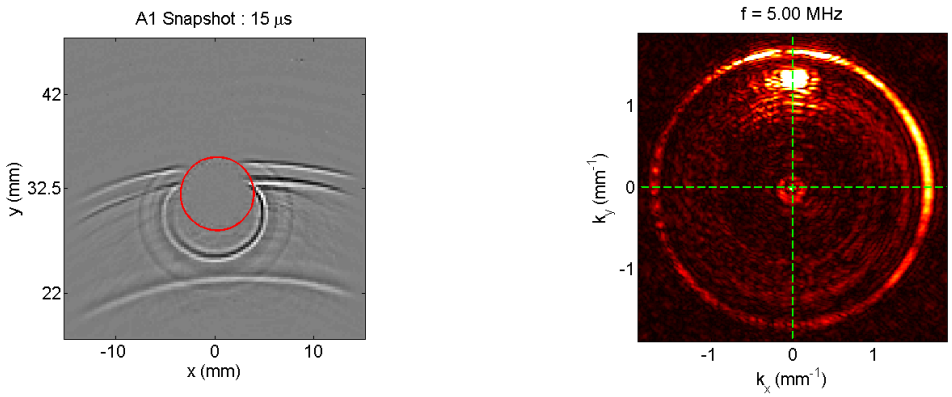

(a) (b)

Figure 4.4: A1 scan slice represented as (a) time-space snapshot at 15 μs and (b) frequency-wavenumber slice at 5 MHz

Table 4.2: Phase velocity ranges.

Wave Mode	Wave Speed (mm/μs)	Phase Velocity (mm/μs)	Range (mm/μs)
Rayleigh	2.9	2.9	$2-3.1$
Shear	3.1	>3.1	$3.1-6.3$
Longitudinal	6.3	>6.3	$6.3-12.8$

velocities of each wave mode. The radial Tukey filters shown in Figures 4.5(b)-4.5(d) are used to create smooth transitions for the Rayleigh, shear, and longitudinal mode filters, respectively, to minimize spectral leakage. These filters are designed and applied to the 2-D wavenumber data for each frequency, and the resulting data are transformed back to the spatial domain via an inverse 3-D FFT.

Although filters for each mode are presented, shear waves are the primary propagation mode of interest in this thesis. Figure 4.6 shows time snapshots of scan A1 decomposed into its three wave modes via phase velocity filtering, with Figure 4.6(c) showing the shear mode.

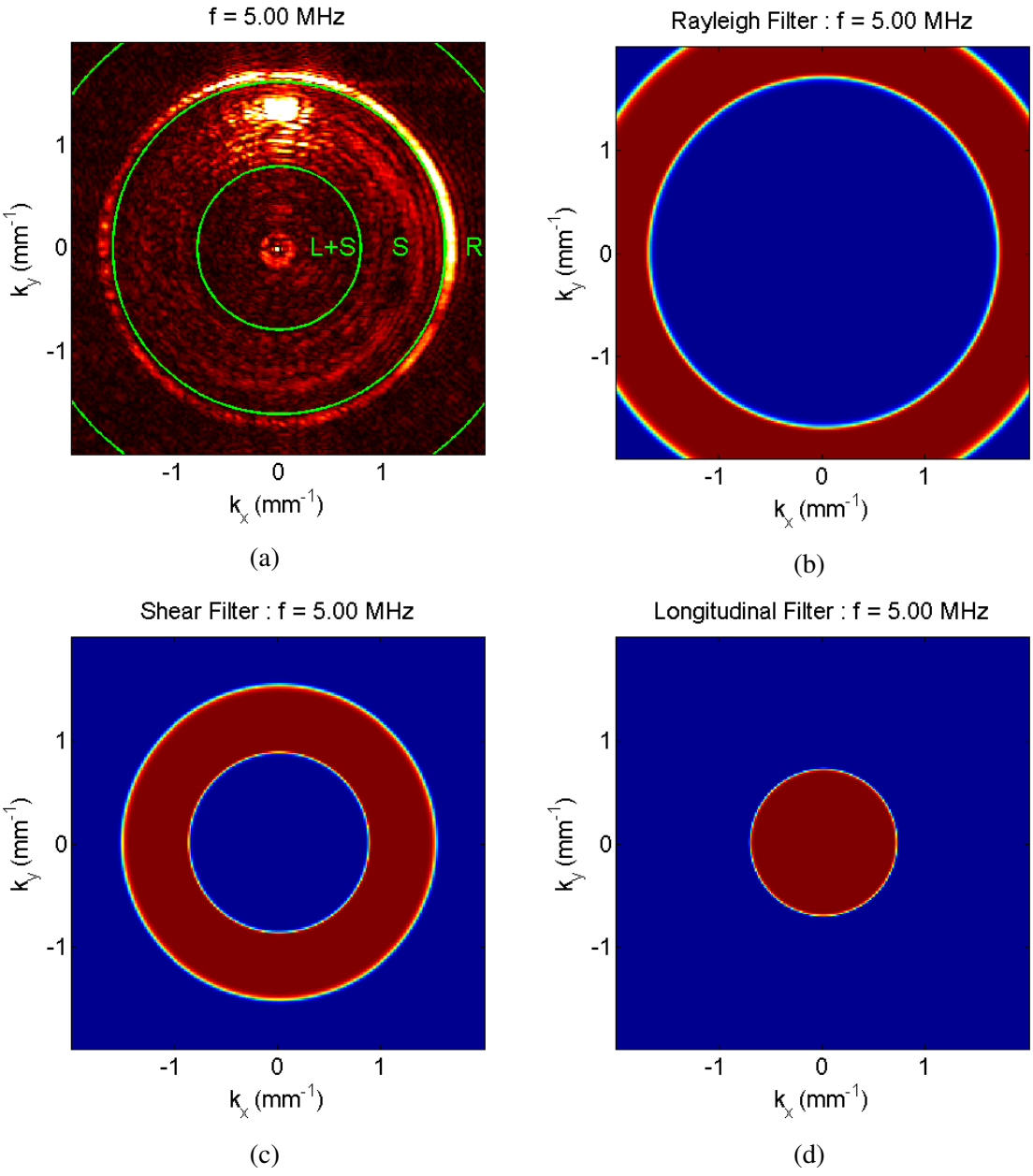

Figure 4.5: Phase velocity filters applied to frequency-wavenumber domain of scan A1 at 5 MHz: (a) slice of 3-D FFT, and (b) Rayleigh, (c) shear, and (d) longitudinal filters

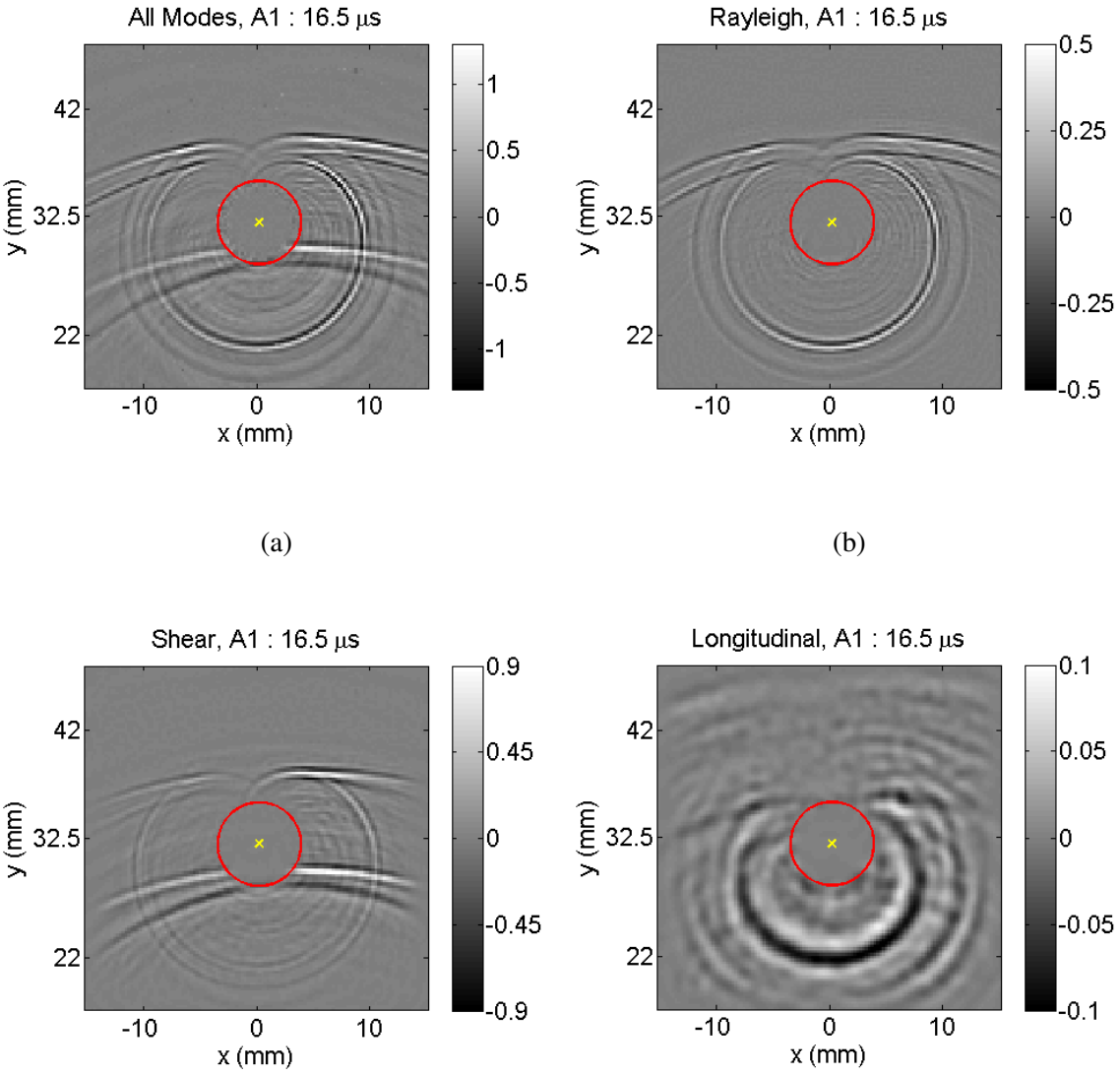

(a) (b)

(c) (d)

Figure 4.6: A1 wavefield snapshots at 16.5 μs of (a) total, (b) Rayleigh, (c) shear, and (d) longitudinal modes

4.6 Directional Filtering

The purpose of directional filtering is to separate waves propagating in a range of directions from the total wavefield. This is illustrated by applying such filtering to the area scan A1 to separate backward-propagating waves from forward-propagating waves. The analysis is in the 3-D frequency-wavenumber domain ω-k_x-k_y. Since backward-propagating waves correspond to the region of the Fourier data where k_y is negative, a window is constructed along the k_y axis that makes a smooth transition from 0 to 1 to separate negative k_y waves from positive k_y waves as shown in Figure 4.7(a). Then, the negative k_y filter is extended to the entire k_x-k_y plane as shown in Figure 4.7(b). A direct multiplication of this k_x-k_y filter and the Fourier data at each frequency extracts the filtered Fourier data for backward-propagating waves, which is shown in Figure 4.7(c) at 5 MHz. To ensure that opposing

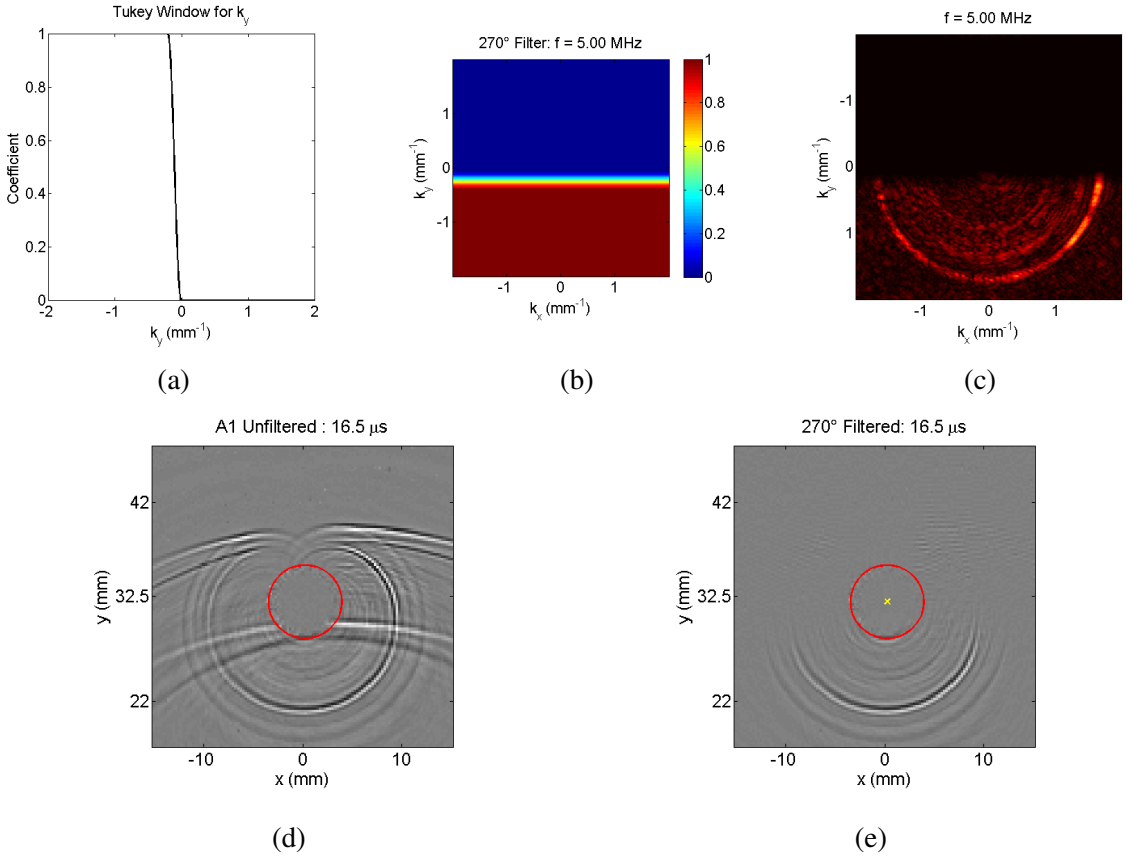

Figure 4.7: Filtering process for forward-propagating waves

waves are removed, the filter can be adjusted by either slightly shifting the filter cutoff in the frequency-wavenumber domain or offsetting the filter direction by a few degrees. Filtered forward-propagating waves can be similarly obtained by a $+k_y$ filter with the appropriate offset applied.

Phase velocity filtering and directional filtering can be combined to further segregate shear wave scattering from a compound scatterer from incident waves; thus, the relative amplitude of element scattering can be improved. Figure 4.8 shows the result of applying phase velocity filtering and directional filtering to segregate notch- and through-hole-scattered shear waves from incident waves in the case of the 4 mm notched through-hole for bonded specimen #3 (scan B8). The notch is oriented at 0° for scan B8, so the resulting notch-scattered waves are approximately centered around the 0° direction. Applying a 0° directional filter to the shear-filtered wavefield retains some incident waves due to the curvature of the wavefront in the x-y plane as shown in Figure 4.8(d). Adding an offset to the angle of the filter, a -15° filter is applied to the wavefield, shown in Figure 4.8(f). Now the incident waves are completely removed with minimal loss of significant scattering information from the notch-scattered shear waves. The use of spatial windowing to further segregate notch scattering from through-hole scattering and notch scattering quantification and analysis is discussed in section 5.

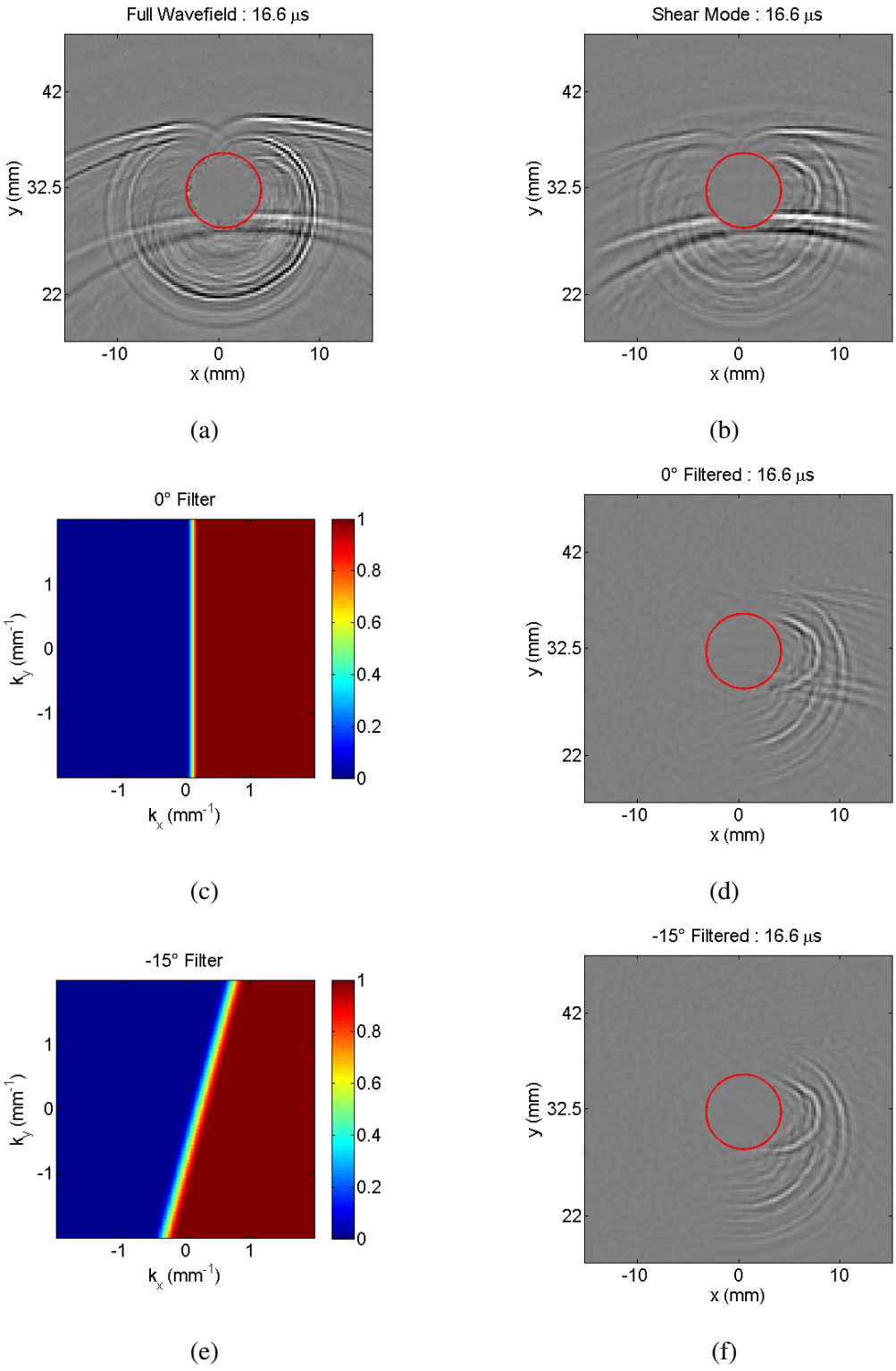

Figure 4.8: Comparison of $0°$ and $-15°$ directional filters

CHAPTER 5
SCATTERING ANALYSIS

As discussed in section 3.2.1, the ultrasonic probe is placed one-and-a-half (1.5) skips away from the scatterer of interest (SOI), where the surface distance is calculated according to the nominal incident angle. However, it is important to note that ultrasonic wave emission does not occur from a single point nor does it propagate as a cylindrical beam. Instead, the ultrasonic incident waves propagate as a diverging beam emitted from the probe, which consists of a contact piezoelectric transducer of 6.35 mm in diameter coupled to an acrylic wedge via an ultrasonic gel couplant. The wedge itself has an elliptical emission face that is coupled to the plate surface. The ultrasonic probe does not emit a perfect "pencil" beam; it can be thought of as a point source that emits multiple rays at a range of angles. The nominal "source", which is located along the center of the ultrasonic beam, has a nominal refracted angle of 56.8° in 6061 aluminum when using a Panametrics ABWM-4T 60° angle-beam acrylic wedge.

In the case of a buried crack-like notch emanating from a through-hole in a bonded specimen, multiple instances of scattering from an SOI can occur from the same excitation due to beam spread. Because incident energy is distributed into a diverging beam rather than a single ray, acquired wavefield images show a number of wave skips according to the angle of incidence, a range of refracted angles, θ_r, and degree of beam spread. The effect of beam spread is clear in line scans as multiple "skips" (wave V-paths) can be seen propagating through the wavefield, shown in Figure 3.7(a). These multiple skips may at first appear to be wavefronts originating from multiple excitations, but recall the data excitation parameters from Section 3.1.3 where a negative spike signal is the only excitation of the plate for a given acquisition window. Instead, multiple skips are generated throughout the plate and appear on the surface as continuous wavefronts due to beam spread.

Due to the placement of the probe, the notch location (i.e., at the far-surface of the top plate, emanating from the through-hole) and the propagation mechanics of bulk waves, incident waves interact with the crack-like defect at odd integer multiples of the half (0.5) skip. Ultrasonic scattering from the SOI at integer multiples of the 1.0 skip is very weak compared to odd integer multiples of the 0.5 skip because the majority of the bulk energy interacts with the through-hole at the top surface (the scanning surface) of the top plate, which is at least 2.35 mm away from the notch. This is primarily due to the placement of the probe (1.5 skips away from the notch location) and the nominal incident angle.

In this section, various methodologies are discussed to quantify scattering from a buried crack-like defect emanating from a through-hole. The first two scattering occurrences, which occur at the 0.5 skip and 1.5 skips, are the primary focus for this work because they contain the most scattering energy in regards to the SOI.

5.1 Wavefield Baseline Subtraction

Wavefield baseline subtraction refers to the process of acquiring baseline (reference) wavefield data from a defect-free specimen and subtracting it from the acquired wavefield data after introducing the defect:

$$r(t, x, y) = w_C(t, x, y) - w_B(t, x, y). \tag{5.1}$$

The residual wavefield, $r(t, x, y)$, is the pixel-wise difference between signals contained in the current wavefield, $w_C(t, x, y)$, and the baseline wavefield, $w_B(t, x, y)$, where all signals are expressed in the 3-D time-space domain. The sensitivity of wavefield baseline subtraction for notch scattering segregation significantly depends on the degree of similarity of incident and through-hole-scattered waves between current and baseline signals [38].

One significant challenge of wavefield baseline subtraction is overcoming the imperfect temporal and spatial alignment of the current and baseline wavefields. Two methods for

aligning the wavefields in space and time prior to performing baseline subtraction have been developed in previous work and are briefly described in this section. The feasibility and results of applying both of these methods to the bonded specimen are also discussed.

5.1.1 Global Space-Time Alignment

The first method of wavefield image registration, global space-time alignment (GSTA), optimally registers the baseline wavefield with the current wavefield by applying subpixel spatial and temporal global shifts [38]. This method is similar to the well-known phase correlation method for aligning images [40] and is used to correct for small shifts in the plate position as well as a constant temporal offset, providing a first order correction for a global temperature change. The GSTA method is accomplished in the frequency domain by minimizing the L2 norm of the residual with respect to $(\Delta t, \Delta x, \Delta y)$, which are the shifts in t, x, and y that are applied to the baseline wavefield prior to subtraction:

$$(\Delta t_0, \Delta x_0, \Delta y_0) = \underset{\Delta t, \Delta x, \Delta y}{\arg\min} \| W_C(\omega, k_x, k_y) - W_B(\omega, k_x, k_y) e^{-j(\omega \Delta t + k_x \Delta x + k_y \Delta y)} \|. \quad (5.2)$$

Here W_B and W_C are the baseline and current wavefield data, respectively, in the ω-k domain and $(\Delta t_0, \Delta x_0, \Delta y_0)$ are the optimal shifts along the three wavefield data dimensions that minimize the L2 norm of the residual. The residual wavefield in the ω-k domain is thus calculated as,

$$R(\omega, k_x, k_y) = W_C(\omega, k_x, k_y) - W_B(\omega, k_x, k_y) e^{-j(\omega \Delta t_0 + k_x \Delta x_0 + k_y \Delta y_0)}, \quad (5.3)$$

which is converted back to the (t, x, y) domain via the inverse 3-D Fourier transform. Both the baseline and current wavefields can be down-sampled in time prior to alignment, which significantly reduces the processing time. The down-sampling does not compromise performance as long as the downsampled sampling frequency is greater than the Nyqiust rate in order to prevent temporal aliasing.

5.1.2 Time Slice Spatial Alignment

The second method of wavefield image registration, time slice spatial alignment (TSSA), spatially aligns each time slice of the current wavefield with a corresponding time slice (frame) of the baseline wavefield prior to calculating the residual wavefield [38]. The frame of the baseline wavefield used for the spatial alignment is selected by looking forward and backward in time by several frames to find the one that is best matched to the current frame after spatial shifts. This method should correct for simple shifts in the plate position as well as small time-varying time shifts, which would provide a second order correction for a temperature change.

This method is performed by first transforming each frame of both the current and baseline wavefields into the k_x-k_y domain via a spatial 2-D Fourier transform (indicated by the overbar). For the n^{th} time slice of the current wavefield, which is at t_n, a range of frames in the baseline wavefield are considered both before and after t_n. The one is selected that minimizes the L2 norm of the residual in the k_x-k_y domain after spatial alignment:

$$(t_n^B, \Delta x_n, \Delta y_n) = \underset{t_k, \Delta x, \Delta y}{\arg\min} \|\overline{W}_C(t_n, k_x, k_y) - \overline{W}_B(t_k, k_x, k_y) e^{-j(k_x \Delta x + k_y \Delta y)}\|, \forall k \in [n_L, n_U]. \tag{5.4}$$

Here n_L and n_U are the lower and upper bounds of the baseline frame index k, and t_n^B is the selected time slice of the baseline wavefield corresponding to the n^{th} time slice of the current wavefield, and $(\Delta x_n, \Delta y_n)$ are the corresponding spatial shifts. The residual wavefield in the k_x-k_y domain at time t_n is thus calculated as,

$$R(t_n, k_x, k_y) = \overline{W}_C(t_n, k_x, k_y) - \overline{W}_B(t_n^B, k_x, k_y) e^{-j(k_x \Delta x_n + k_y \Delta y_n)}, \tag{5.5}$$

which is converted back to the (t, x, y) domain via an inverse 2-D Fourier transform at each time step. By performing the optimal spatial alignment on a frame-by-frame basis

and by allowing some play in the correspondence between frames in the two wavefields, the alignment is more robust to environmental variations such as a temperature change. As a note, the temporal sampling of the two wavefields does not have to be the same to use the TSSA method. Just as for GSTA, the current and baseline wavefield sampling rates can be down-sampled prior to alignment as long as the Nyquist rate is adhered to. Finer sampling interval for the baseline improves the performance of TSSA by increasing the resolution of the frames available for matching.

5.1.3 Application to Bonded Specimen

As discussed, a bonded specimen was fabricated from two isotropic plates using an epoxy bonding method. The inclusion of buried defects with varying geometries adds an increased level of specimen complexity; the bonded specimen poses additional challenges to both fabrication and analysis as compared to a single plate. In particular, the defect in the form of a buried notch emanating from a through-hole must be machined before the second plate is bonded to the first. Thus, it is not possible to acquire a damage-free baseline wavefield from the same through-hole that has the notch. The approach taken here is to acquire a baseline wavefield from a nominally identical through-hole in the same bonded specimen but that does not have a notch. An additional issue is that the wavefields acquired from the bonded specimen are more complex than the corresponding ones from a single plate because of the waves propagating in the second plate. The complicated scattered wavefield contains information regarding several different specimen features, yet extracting this information and correctly identifying its relation to physical events are very difficult.

Figures 5.1(a) and 5.1(b) show wavefield frames at 17.32 μs of the damaged and undamaged through-holes for the bonded specimen from scans B1 and B2. Clear scattering from the notch can be visualized easily in the time-space domain in Figure 5.1(a) as compared to the frame of Figure 5.1(b) from the undamaged hole. Figure 5.1(c) shows the corresponding residual frame after direct baseline subtraction without any alignment, and

completely fails to isolate the notch-scattered waves from the total wavefield. It can be seen that both the incident and hole-scattered waves have actually become larger, indicating that neither is lined up sufficiently for successful suppression via baseline subtraction.

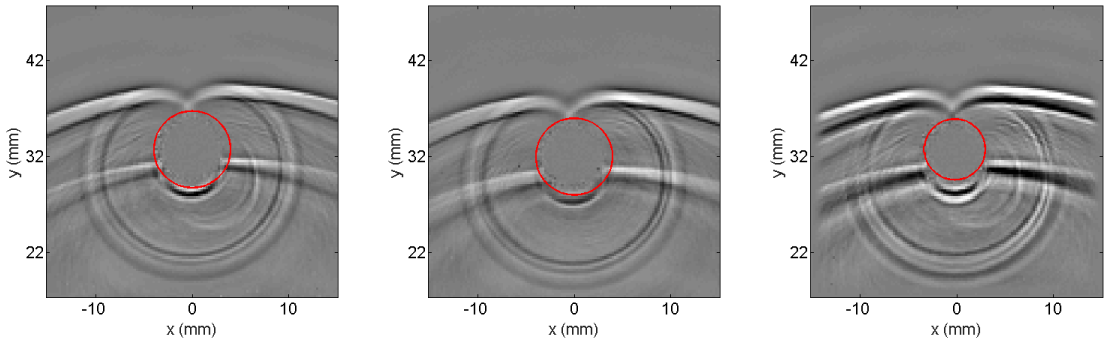

(a) (b) (c)

Figure 5.1: Wavefield snapshots from bonded specimen #1: (a) current, (b) baseline, and (c) residual after direct subtraction

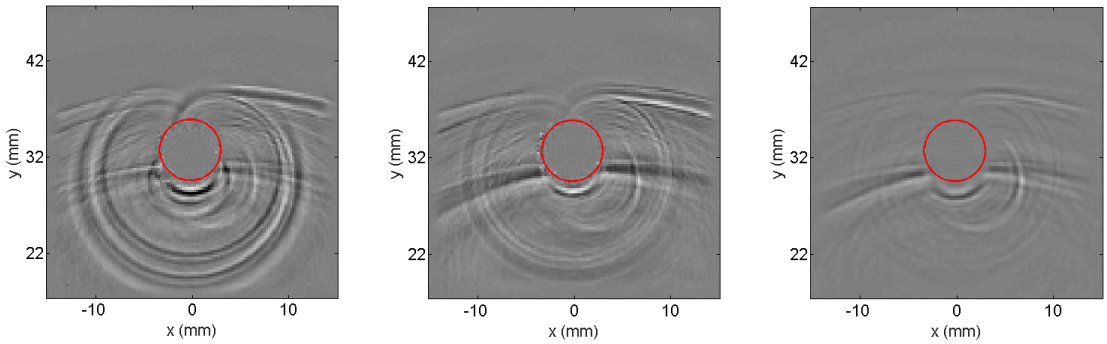

(a) (b) (c)

Figure 5.2: Residual snapshots from bonded specimen #1: (a) after GSTA, (b) single frame TSSA alignment, and (c) single frame TSSA after shear wave filtering

Figure 5.2 shows residual snapshots after application of three different baseline subtraction methods. Figure 5.2(a) is the 17.32 μs snapshot after applying GSTA. This global alignment method does improve the ability of baseline subtraction to reduce the incident waves, but the hole-scattered waves are still quite large in amplitude. Figure 5.2(b) shows the same snapshot but after performing TSSA alignment on only one frame. That is, the

Table 5.1: Baseline subtraction performance for bonded specimen.

Alignment Method	Mean Residual Energy (dB)	Peak Residual Energy (dB)
None	-12.9	4.2
GSTA	-18.9	1.3
Single Frame	-20.9	-2.4
Single Frame+c_p Filter	-23.5	-2.5

baseline snapshot was spatially shifted to best match the same frame of the current wavefield according to the TSSA methodology. There are fewer artifacts than after GSTA, but the notch-scattered waves are still dominated by feed-through of the incident and hole-scattered waves. The same TSSA, single-frame alignment procedure was implemented after phase velocity filtering to keep only shear waves, and that result is shown in Figure 5.2(c). Although there is some further reduction in artifacts, the notch-scattered waves are still not sufficiently isolated.

Table 5.1 summarizes performance for all of the baseline subtraction methods implemented. The mean and peak residual energies for the four cases are computed for the single frame at 17.32 μs relative to the mean and peak energies of the single baseline frame. As expected, performance is improved as alignment and filtering steps are added, but is still inadequate to characterize notch scattering.

The primary reason that baseline subtraction fails is that, unlike the results reported by Dawson *et al.* [38], the baseline data from the undamaged hole were recorded from a different through-hole than the notched hole data. As previously explained, the specimen fabrication procedure required that the notch be introduced prior to bonding the second plate to the first, resulting in a buried defect. Thus, the baseline wavefield data had to be acquired from an undamaged through-hole different from the notched through-hole. Not only was a global shift in the plate possible, it was also likely that the transducer position relative to the through-hole was not identical for the two scans. Given that the shear wavelength at 5 MHz is on the order of 0.5 mm, even small offsets in transducer

placement will yield significant changes in the phase of the resulting wavefield. These changes, combined with unavoidable variations in coupling and machining, result in the failure of baseline subtraction to isolate the notch-scattered waves. It may be possible to obtain better baseline subtraction results by first using directional filtering to remove the incident waves, and then considering a range of baseline frames to try to better match the notch-scattered waves.

5.2 Radial Energy

The time-space domain presents wavefield propagation and scattering data in an intuitive and qualitative way, but it is difficult to quantify scattering without further processing in other domains. Scattering is quantified here by generating energy curves as a function of a scattering direction, denoted the observer direction. Four scattering quantification methods are discussed: full radial energy, snapshot radial energy, time-windowed radial energy and space-windowed radially energy. In this section, the observer direction methodology for defining radial energy is first defined and discussed. Then each method for calculating radial energy is presented and applied to acquired wavefield data from selected scans. Finally, results and observations for each case are presented.

5.2.1 Observer Direction

The scattering direction for energy calculations can be defined in multiple ways; however, only one definition of direction is considered here: the observer direction. Kummer explains the differences between observer and propagation directions, each of which may be used for scattering quantification [39]. The observer direction is defined in the time-space domain and is relative to a specific reference point for radial energy integration paths. For the work reported here, the reference point is the hole center, although that is not a requirement. The observer direction is defined radially outward from the reference point using the standard definition of a polar angle in two dimensions; 0° refers to the direction horizontally

to the right and the angle increases counterclockwise. Given the definition of the observer direction, the goal is to quantify scattered energy as a function of polar angle. However, only defect-scattered waves are of interest, which raises the problem of segregating SOI scattering from the total wavefield. It was discussed earlier that while baseline subtraction works for very controlled experiments, it is not robust enough to handle the bonded specimen scans (B-series). Instead, a combination of frequency-wavenumber (mode and directional) filtering and spatial windowing are applied to segregate defect scattering from a compound scatterer.

5.2.2 Full Radial Energy

Full radial energy calculations utilize the observer direction definition to obtain scattering patterns. The energy for a range of directions is calculated by integrating over regions defined by lower and upper bound phase velocity boundaries in ω-k space.

Figure 5.3 illustrates the processing steps to extract and quantify notch-scattered waves using the full radial energy methodology. As an example, this process is applied to scan A3, an area scan of a single 6.35 mm-thick plate containing a through-hole with a 4 mm EDM notch emanating from the far surface. The data are first processed using shear phase velocity and -15° directional filters. The C-scan is then radially interpolated outward from the hole center along a line, starting at a radius of 4 mm (hole window boundary) and ending at a radius of 13 mm (scan area boundary) as shown in the snapshot of Figure 5.3(a). The wavefield is thus converted from rectangular coordinates (t, x, y) into polar coordinates $(t, r; \theta_0)$, where the angle θ_0 is the observer direction. Figure 5.3(b) shows the radial line scan for $\theta_0 = 270^\circ$ (below the hole). Each radial line scan is transformed into the 2-D frequency-wavenumber domain $(\omega, k_r; \theta_0)$ via the 2-D FFT. Figure 5.3(c) shows the corresponding frequency-wavenumber slice for $\theta_0 = 270^\circ$. Signals distributed in the first and third quadrants correspond to outward propagating waves relative to the reference point (the hole center) in the time-space domain. In contrast, signals located in the second

and fourth quadrants correspond to the inward propagating waves. Energy accumulation of signals distributed in the first quadrant in each frequency-wavenumber slice (each θ_0) leads to scattered energy curves as a function of observer direction as shown in Figure 5.3(d). The following list details the processing steps for the full radial energy methodology:

1. Apply a 20% Tukey window in time between 1 and 30 μs.
2. Apply a 20% Tukey window in x and y to smooth the outer edges.
3. Apply a 6th order circular Butterworth window with a 4 mm radial cutoff to suppress through-hole noise for the 6.35 mm diameter hole
4. Transform wavefield data to the 3-D frequency-wavenumber domain via the 3-D FFT.
5. Apply a 33% Tukey window in frequency between 0.5 and 6.5 MHz to eliminate any spatial aliasing.
6. Apply phase velocity filtering to extract the shear mode described in section 4.4 using a 33% Tukey window between wavenumber boundaries at each discrete frequency.
7. Apply -15° directional filter using a 33% 2-D Tukey window in the wavenumber-wavenumber domain for all frequencies
8. Transform back to the time-space domain via the inverse 3-D FFT.
9. Radially interpolate the reconstructed shear wavefield for directions of 0° to 360° at a 1° angular increment and from 4 mm to 13 mm with a 0.1 mm radial increment.
10. Transform each radial B-scan to the 2-D frequency-wavenumber domain via the 2-D FFT.
11. Accumulate energy in the first quadrant for each angle to build energy curves as a function of angle (i.e., the observer direction).

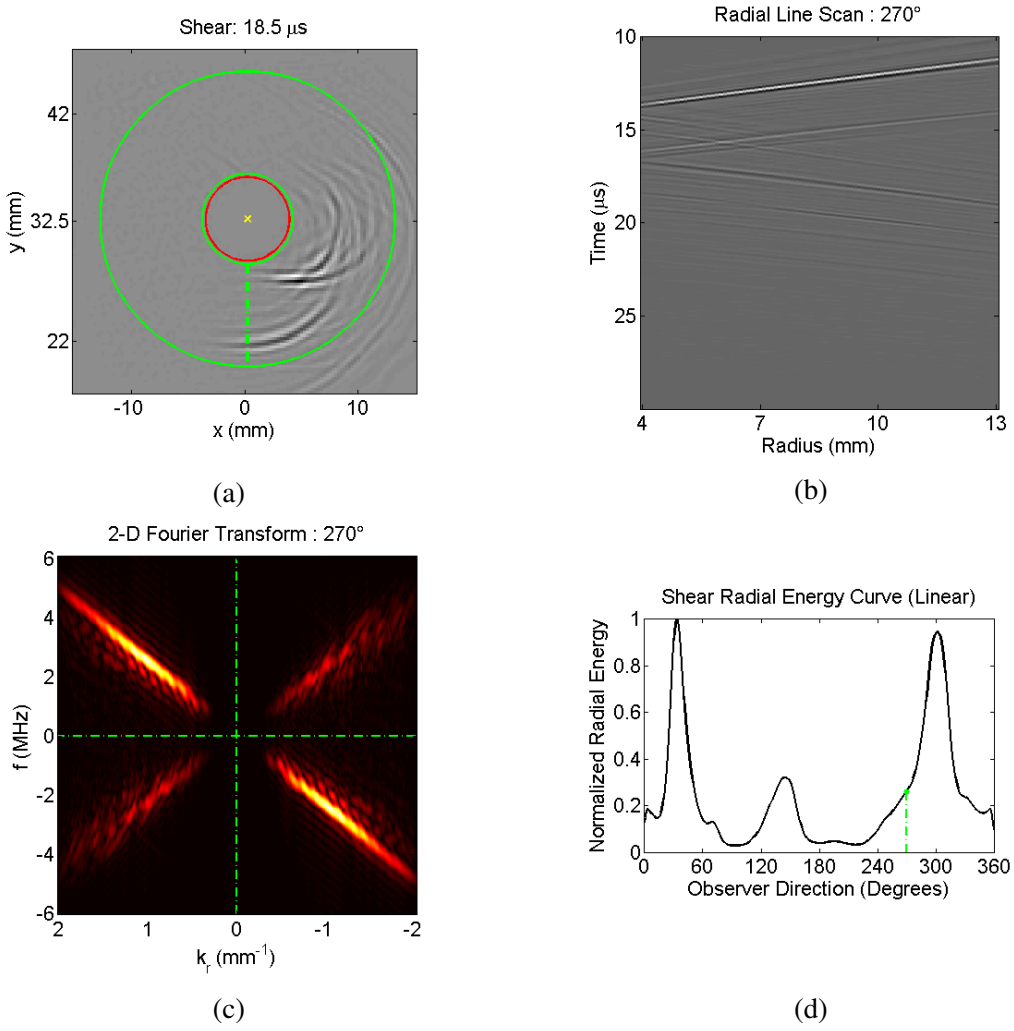

Figure 5.3: Quantification of shear wave scattering via the full radial energy method

Figure 5.3(d) shows the resulting scattering pattern generated using the full radial energy method. Because energy is summed in the frequency-wavenumber domain, detailed temporal information is lost in this calculation method. Furthermore, relatively low energy scattering phenomena are obscured by dominating incident energy.

Figure 5.4 shows the full radial energy curves and scattering patterns for scans A1-A3 and B6-B8, which were recorded from single (A1-A3) and bonded (B6-B8) plate specimens. Recall from Table 3.2 that A1 and B6 are scans of the undamaged through-hole while A2, B5 and A3, B8 are scans of the 2 mm EDM notched-hole and 4 mm EDM notched-hole, respectively. All scan data were pre-processed with shear mode filtering and

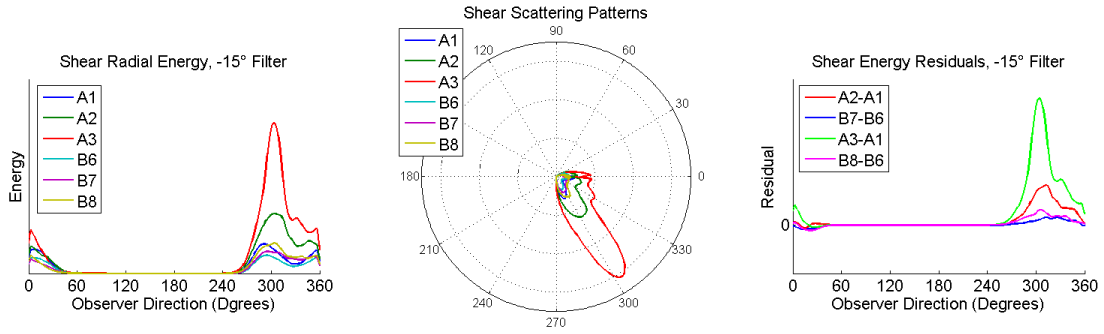

(a) (b) (c)

Figure 5.4: Quantified shear wave scattering displayed in (a) rectangular and (b) polar representations and (c) as energy residuals

$-15°$ directional filtering. It is immediately apparent from Figure 5.4(a) that the bonded specimen (B-series) scans have lower radial energy than the single plate (A-series) scans across all directions. The reduction in energy across all angles and the fact that scans A1-A3 and B6-B8 were all acquired using the same experimental settings indicates that energy leakage is occurring at the bonding interface near the through-hole. Despite the lack of detailed information on specific notch-scattering, the compounded backscattered energy increases from scans A1 (no notch) to A2 (2 mm notch) to A3 (4 mm notch). It is likely that the increased defect size is directly attributing to the increase in backscattered energy. As a result, forward-scattered energy decreases with the introduction of the notch. These trends continue with the B6-B8 scans albeit with lower intensity (i.e., the increase in backscattering energy from scan B6 to B7 to B8 is less than in the single plate specimen). Although it is true that the increase in backscattered energy positively correlates with the increase of defect size, full radial energy calculations do not give enough detail for robust defect scattering quantification.

Residual energy curves were also generated by direct subtraction as shown in Figure 5.4(c). Although direct wavefield baseline subtractions do not produce valuable residual wavefields, direct energy residuals can provide intuitive information about the differences between current and reference wavefields due to notch scattering via positive (i.e., > 0)

and negative (i.e., < 0) values. Ideally, positive values would imply notch scattering, and negative values would be indicative of shadowing as manifested by a decrease in energy moving from the reference to the current wavefield.

Figure 5.4(c) shows that increasing notch lengths yield greater backscattering for both single and bonded specimens. Subsequently, forward scattering energy decreases from reference to current wavefields. Although the reference and current wavefields were carefully measured under very similar experimental conditions, it is not entirely clear whether the positive residual curves in Figure 5.4(c) correspond to notch scattering alone or a combination of notch and through-hole scattering. Small deviations in the direction of through-hole scattering between reference and current wavefield scans, which can be caused by unintentional probe displacement, can lead to residual energy curves that are not representative of notch scattering alone. This is particularly true for full radial energy calculations since temporal information is lost, and small spatial deviations of through-hole scattering on a frame-by-frame basis are lumped together over the entire 30 μs window, resulting in potentially significant through-hole spatial discrepancies. Performing a direct energy subtraction under these circumstances could yield inaccurate representations of notch scattered energy in both the forward and backward scattering directions.

5.2.3 Snapshot Radial Energy

One reason for the lack of detail in full radial energy calculations is the loss of temporal information from energy summing along phase velocity areas; a natural solution is to generate the radial energy curves in the time-space domain instead. Snapshot radial energy calculations (denoted in Eq. 5.6 as SRE) generate radial energy curves for a single wavefield frame, called a snapshot. The snapshot is picked to represent the subjective maximal scattering from the SOI. The subjective maximal is simply the wavefield frame that has the "best" scattering from the SOI in terms of its separation from the other element of the compound scatterer and the relative strength of the scattering wavefront. Such snapshots could

potentially be chosen automatically but here were manually identified. Energy summing for a particular snapshot in the spatial domain is done by

$$\mathrm{SRE}(\theta) = \sum_j w(r_j, \theta)^2. \tag{5.6}$$

Figure 5.5 shows the wavefield snapshot at 16.6 μs for each scan with all plots shown on the same gray scale, and Figures 5.6 and 5.7 show the corresponding snapshot radial energy curves for scans A1-A3 and B6-B8, respectively, that were pre-processed with shear mode filtering and -15° directional filtering. The 16.6 μs snapshot was chosen based on the "best" half (0.5) skip for observed 4 mm notch scattering; a "best" scattering frame for the 2 mm notch scattering could not be identified. Comparing the radial energy scales in Figures 5.6(a) and 5.7(a), it appears that energy leakage has occurred in the second layer of the bonded specimen due to the reduction of energy across all angles compared to the single plate scans. The energy curves in Figure 5.6(a) provide more intuitive detail than the full radial energy method by showing scattering energy resulting from the compound scatterer at the 16.6 μs scattering frame, which corresponds to 0.5 skip notch scattering.

The residual curves of Figure 5.6(b) indicate that maximal notch scattering occurs at about 0° in the 4 mm case of the single plate specimen, and Figure 5.7(b) suggests maximal notch scattering occurs at around 15°, both of which approximately correspond with the orientation of each notch. The 2 mm notch, however, does not appear to produce significant scattering in the forward direction as compared to the 4 mm notch; in fact, the 2 mm notch residual in Figure 5.7(b) has a negative residual indicating that more forward scattering energy in the 0° to 50° range occurs in the reference wavefield than in the current wavefield. The presence of greater backscattered energy in the more direct backscattering direction (i.e., closer to 270°) could imply that notch scattering loss occurs in the forward scattering direction because the notch prevents through-hole scattering from propagating in the forward direction. Interestingly, this trend does not occur in the 4 mm notched-hole

case, implying that changes in notch length have a more complicated effect on notch scattering than simply increasing the backscattered energy. Although the backscattered total energy summed across all directions increases from the 2 mm to 4 mm notched-hole cases in bonded specimen #3, the distribution of energy changes. A similar trend appears to occur between the 2 mm and 4 mm notched-hole cases for the single plate in Figure 5.6(a), but it is difficult to tell if the energy is redistributed in a similar way as observed in Figure 5.7(a). Another complicating factor is that the snapshot time was chosen based on scattering from the 4 mm notch, not the 2 mm notch.

The notch scattering at one-and-a-half (1.5) skips is not fully separated from through-hole scattering in the time-space domain as shown in Figures 5.8, where each plot is shown on the same gray scale. The snapshot time, 18.8 μs, was chosen based on the "best" 2 mm notch scattering for the 1.5 skip. Figures 5.9(a) and 5.10(a) show radial energy curves for the stronger and spatially overlapped 1.5 skip notch scattering for both single and bonded plates, respectively. Due to the spatial overlap of notch-scattered and through-hole scattered waves, energy curves in the $-30°$ to $60°$ observer direction range contain lumped

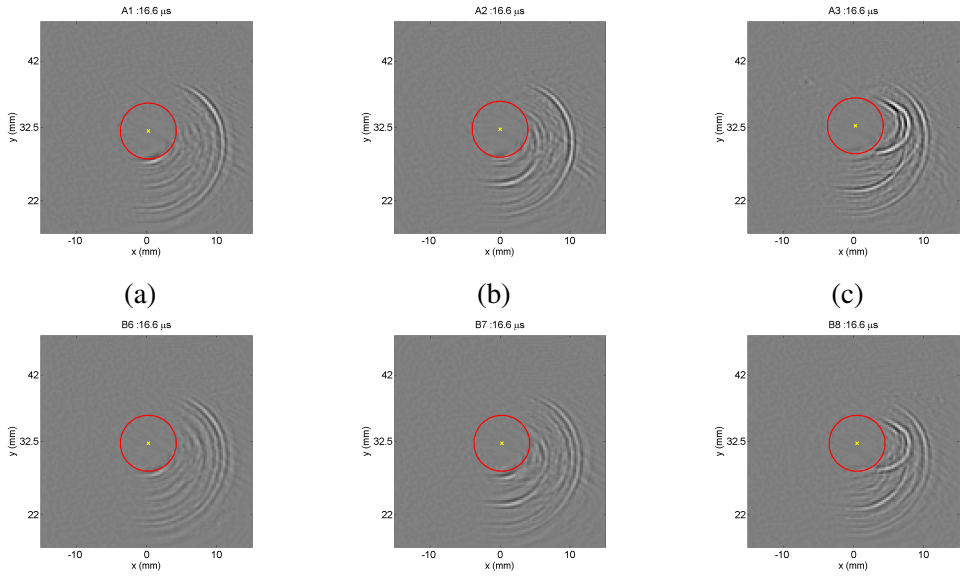

Figure 5.5: 16.6 μs wavefield snapshots for scans A1-A3 and B6-B8 with phase velocity and $-15°$ directional filtering

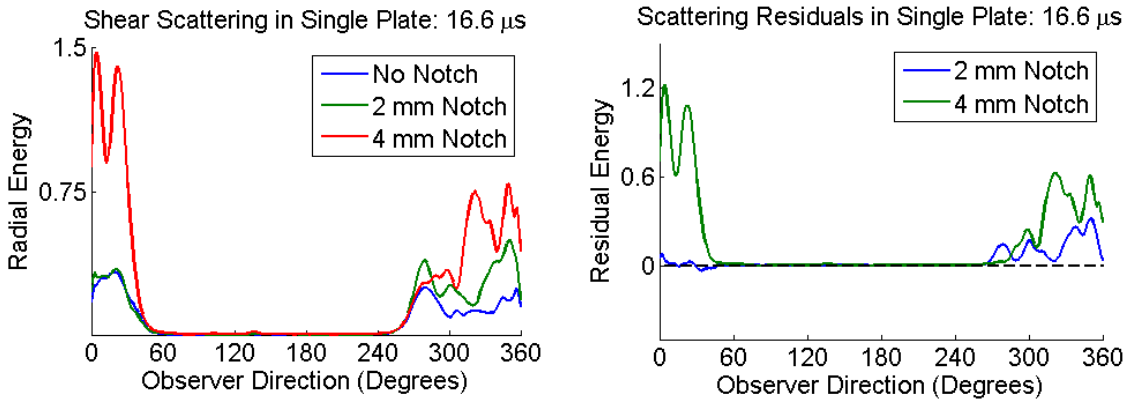

(a) (b)

Figure 5.6: Radial energy analysis for 0.5 skip scattering in the single plate specimen with (a) snapshot radial energy curves and (b) residual energy

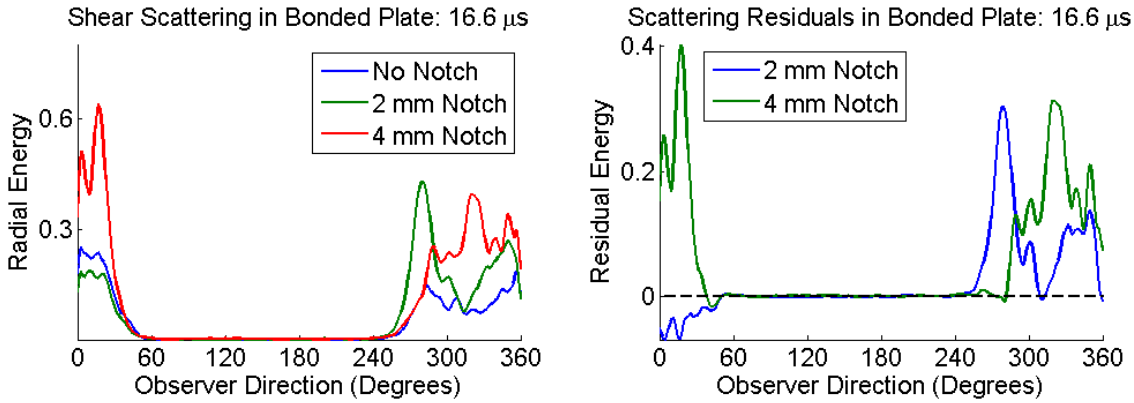

(a) (b)

Figure 5.7: Radial energy analysis for 0.5 skip scattering in bonded specimen #3 with (a) snapshot radial energy curves and (b) residual energy

scattering energy from both the notch and through-hole. Figures 5.8(b) and 5.8(c) show notch-scattering separation in the 18.8 μs frame near the 320° scattering direction. Spatial windowing can be used to segregate and independently quantify the notch scattering for a

narrower observer direction range in the 2 mm and 4 mm notched-hole cases for the single plate specimen, but only a small portion of the notch scattering lobe would be quantified because the notch scattering lobe is largely overlapped with through-hole scattering.

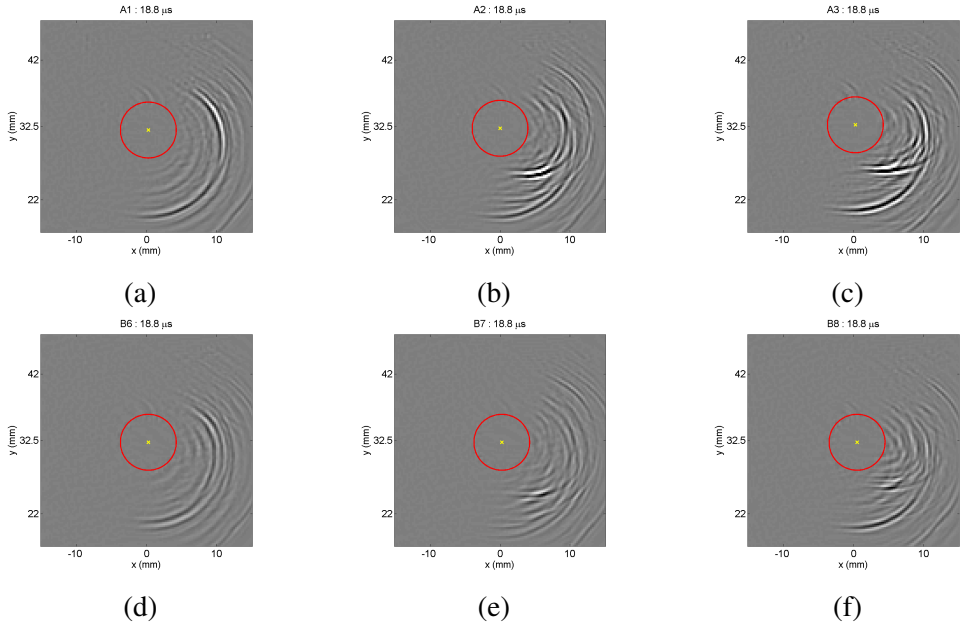

Figure 5.8: 18.8 μs wavefield snapshots for scans A1-A3 and B6-B8 with phase velocity and -15° directional filtering

Alternatively, residual energy can be used to show the difference between current and reference wavefields for each observer direction. Different from the 0.5 skip behavior, residual curves in Figures 5.9(b) and 5.10(b) indicate that scattering energy is distributed similarly between the 2 mm and 4 mm notched cases for both the single and bonded plate specimens. 4 mm notch scattering in both the single plate and bonded specimens has higher amplitude backscattering, which is expected considering the 1.5 skip. Furthermore, the ratio of notch backscattering energy to forward scattering energy loss (negative residual) is higher in the single plate specimen than in the bonded specimen. This likely indicates that the addition of a second layer reduces the amount of notch-scattered energy that returns to the top (scanned) surface.

1.5 skip scattering in Figures 5.8(e) and 5.8(f) is not as clean as the 0.5 skip scattering in Figures 5.5(e) and 5.5(f), but it appears as though the notch-scattering lobes in Figure

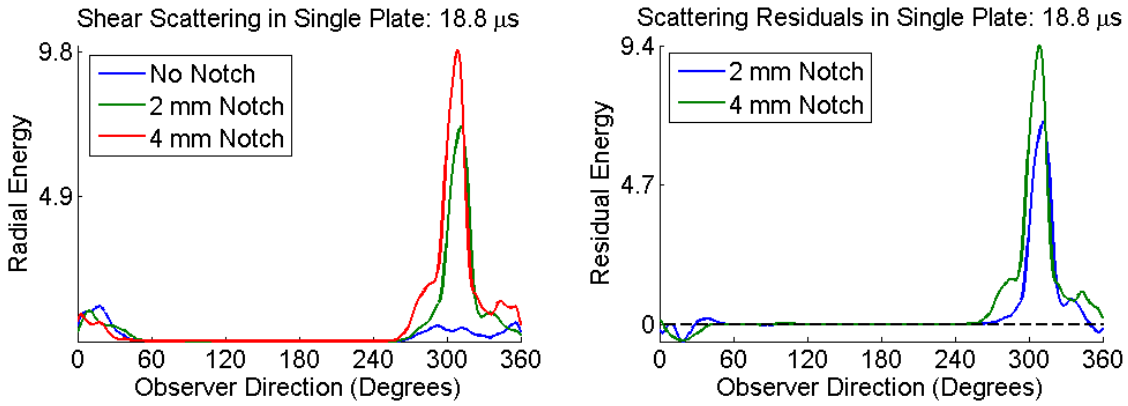

(a) (b)

Figure 5.9: Radial energy analysis for 1.5 skip scattering in the single plate specimen with (a) snapshot radial energy curves and (b) residual energy

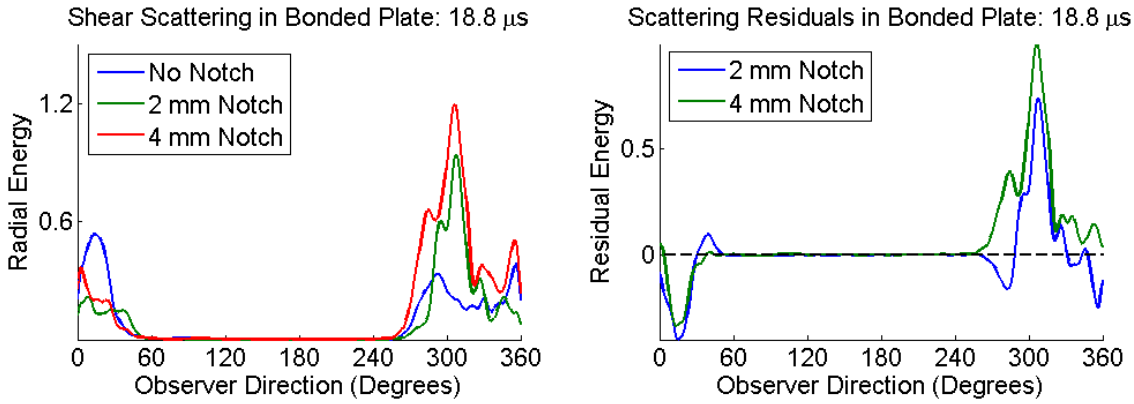

(a) (b)

Figure 5.10: Radial energy analysis for 1.5 skip scattering in bonded specimen #3 with (a) snapshot radial energy curves and (b) residual energy

5.10(b) are larger than those in Figure 5.7(b). This makes sense because notch scattering from the 1.5 skip should be greater in amplitude than 0.5 skip notch scattering since it corresponds to the nominal refracted angle of shear wave energy. The wider scattering

lobe for the 4 mm notch at 1.5 skips combined with potential phase cancellation between overlapped through-hole and notch-scattered waves in Figure 5.8(f) could be the cause of the shift in maximal notch-scattering direction between the 0.5 and 1.5 skips. Notch shadowing can also be seen in Figure 5.10(b) indicated by the negative residual energy lobe oriented around 20°.

As shown in Figures 5.6, 5.7, 5.9 and 5.10, snapshot radial energy provides greater detail for specific element scattering in a compound scattering scenario than full radial energy processing. However, the gain in detail comes at a cost as this method of radial energy calculation only generates energy curves for a single frame.

Bonded Specimen #2

Combining directional filtering and snapshot radial energy is particularly useful for analyzing notch scattering for bonded specimens because notch scattering energy is lower in the bonded plate scans than in the single plate scans. Directional filtering is used to segregate waves propagating at -45° from the rest of the wavefield; the filter used for the second bonded specimen is shown in Figure 5.11(b). It is clear in Figure 5.11(c) that directional filtering is particularly useful for removing unwanted incident waves so that better notch scattering quantification can be done. The rest of this section applies the snapshot radial energy analysis to the second bonded specimen (scans B3-B5), and notch scattering due to the 0.5 skip incident wave is analyzed.

Two separate snapshots were chosen for the radial energy analysis for 0.5 skip scattering because the "best" scattering frame for the 2 mm and 4 mm notches occurs at different time snapshots. At 16.6 μs, 2 mm notch scattering (scan B4) is weak and not well visible in the time-space domain as shown in Figure 5.12(b). 4 mm notch scattering is visible at this snapshot, but it is not separated from through-hole backscattering, shown in Figure 5.12(c). Despite its lack of time-space separation from through-hole backscatter, 4 mm notch scattering appears to reach a maximum near 300° in Figure 5.13. The residual curves

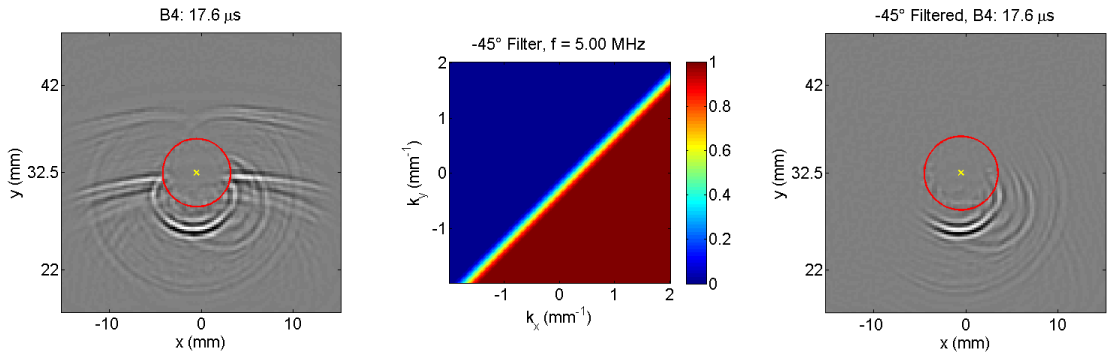

(a) (b) (c)

Figure 5.11: $-45°$ directional filtering applied to the 2 mm notched-hole in bonded specimen # 2 (scan B4); plots displayed on the same color axis

in Figure 5.13(b) present conflicting information; significant negative and positive residuals exist in both forward- and backscattering directions. This could be indicative of through-hole wave backscatter misalignment between scans B3 and B5, but it is not clear. The 4 mm notch residual (B5-B3) does show a maximum positive residual near the same observer direction as the maximal backscatter in Figure 5.13(a), but it also shows a negative peak residual of near equal magnitude roughly $20°$ from the maximum positive residual.

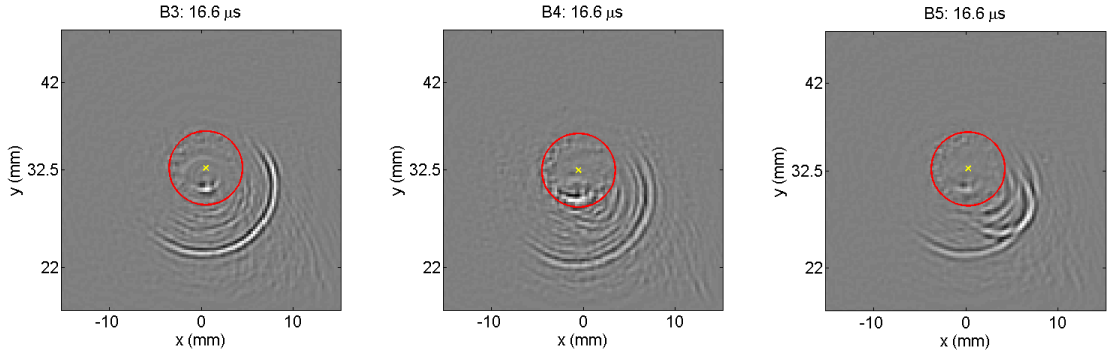

(a) (b) (c)

Figure 5.12: 16.6 μs wavefield frame for scans B3-B5, displayed on the same color axis

At 17.6 μs, 0.5 skip notch scattering from the 2 mm notched-hole is separated in space and time from through-hole scattering, shown in Figure 5.14(b), making it an ideal scenario for scattering analysis. Figure 5.15(a) shows the relative strength of backscattering in scan

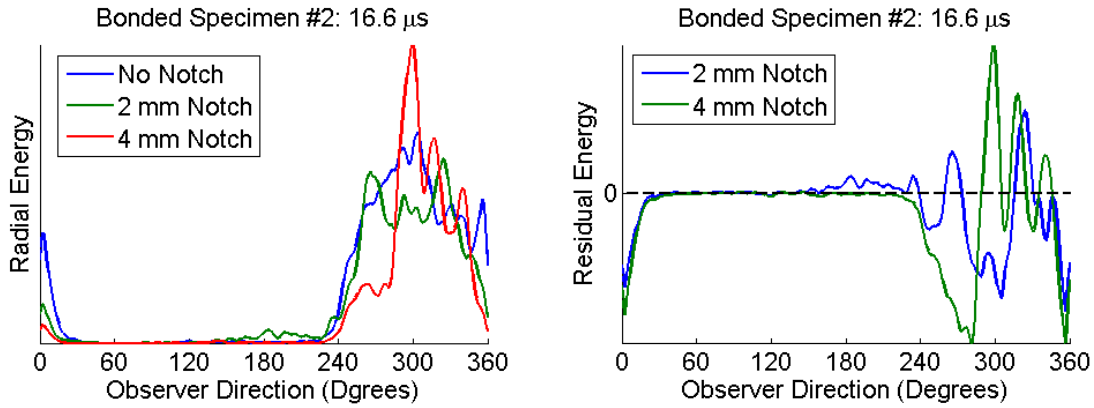

(a) (b)

Figure 5.13: Radial energy analysis for 0.5 skip scattering in bonded specimen #2 with (a) snapshot radial energy curves and (b) residual energy

B4 compared to both the no notch and 4 mm notch cases. However, according to Figure 5.15(b), the majority of the backscatter in the 2 mm notch case appears to come from the through-hole ($270°$) and not the notch (around $315°$). Again, this may be due to small probe displacements in either x or y directions. The local maximum at $315°$ is likely indicative of notch scattering, as this observer direction corresponds with the $-45°$ notch orientation.

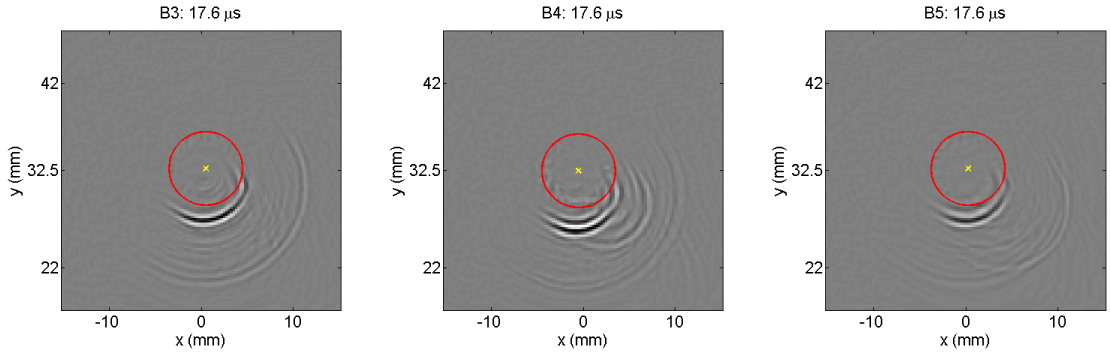

(a) (b) (c)

Figure 5.14: 17.6 μs wavefield frame for scans B3-B5, displayed on the same color axis (different from the color axis of Figure 5.12)

Because 0.5 skip notch scattering occurs at such different times for the 2 mm and 4 mm

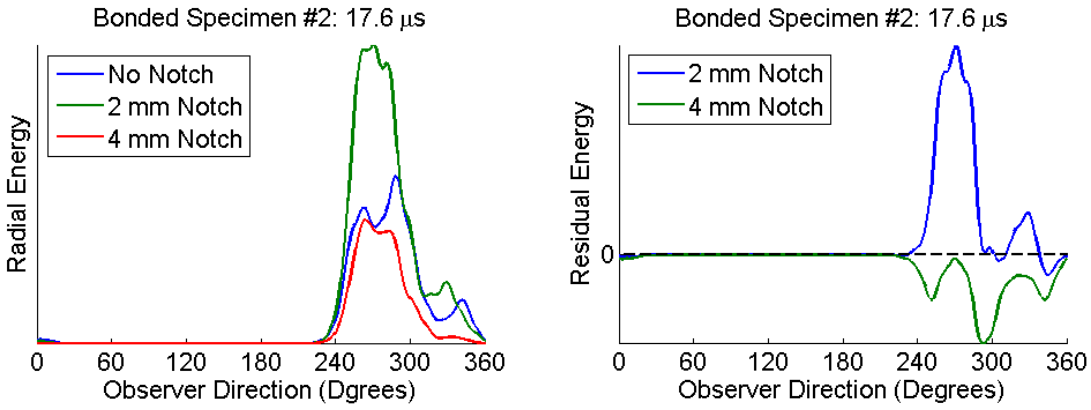

(a) (b)

Figure 5.15: Radial energy analysis for 1.5 skip scattering in bonded specimen #2 with (a) snapshot radial energy curves and (b) residual energy

notch cases, it is difficult to select a single scattering frame to compare both wavefields. In the 16.6 μs snapshot 2 mm notch scattering appears to have not reached the top surface yet and therefore does not appear in the wavefield, yet 4 mm notch scattering is visible because it arrives to the surface near the same time as the through-hole backscatter. Furthermore, 2 mm notch scattering is time-space separated from through-hole backscatter in the 17.6 μs frame, but 4 mm notch scattering has already dissipated since it was overlapped with through-hole backscatter. Since the equipment used for acquisition only measures the top surface of each specimen, interactions in the bulk are not quantified experimentally and the precise cause for the delay in 2 mm notch scattering is not known. However, it is likely related to incident waves diffracting from the upper edge of the notch, which is further from the top surface (i.e., the scan surface) of the plate for the 2 mm notch as compared to the 4 mm notch. Thus, waves must travel further from the transducer to the upper notch-through-hole connection point to the top surface in the 2 mm notch case than in the 4 mm notch case.

5.2.4 Time-Windowed Radial Energy

Time-windowed radial energy combines the methodologies of full and snapshot radial energy processing by generating radial energy curves for a range of frames over a specified temporal window. Time-windowed radial energy (denoted in Eq. 5.7 as TWRE) is calculated in the discrete time-space domain as:

$$\mathrm{TWRE}(\theta) = \sum_i \sum_j w(t_i, r_j, \theta)^2. \tag{5.7}$$

Using this formulation, radial energy can be calculated and displayed for a range of individual scattering frames or summed across the entire time window for a result equivalent to full radial energy. Snapshot radial energy can also be generated from this formulation by excluding the summation over the time index, i, and instead selecting a particular frame.

Figures 5.16 and 5.17 show the radial and residual energy curves for a time window of 16 μs to 19 μs for the single plate and third bonded specimens, which were pre-processed with shear mode filtering and -15° directional filtering. The decrease in energy across all observer directions from the single plate specimen to the bonded specimen remains consistent as evident in the comparison of Figures 5.16(a) and 5.17(a). The residual energy curves in Figures 5.16(b) and 5.17(b) follow similar trends as the full radial energy for single and third bonded specimens in Figure 5.4(c), but time windowing the energy calculation to focus on notch scattering appears to add more detail to all of the residual curves. The maximal residual is also likely to correspond more directly with notch scattering since through-hole backscatter in similar directions that would occur after the time window (16 μs to 19 μs) are not included in the energy calculations; however, lumped time-windowed radial energy provides less intuitive results than snapshot radial energy because the energy curves represent scattering effects over a range of snapshots and not just for a single scattering frame.

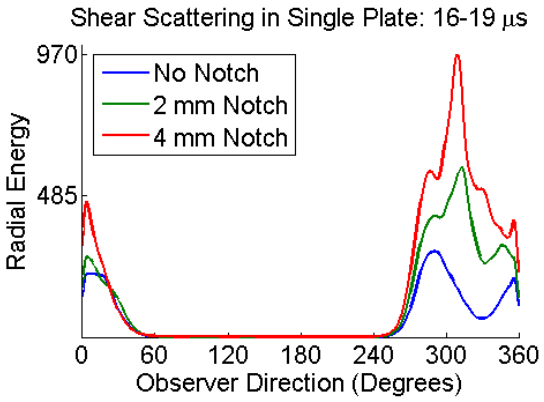

(a)

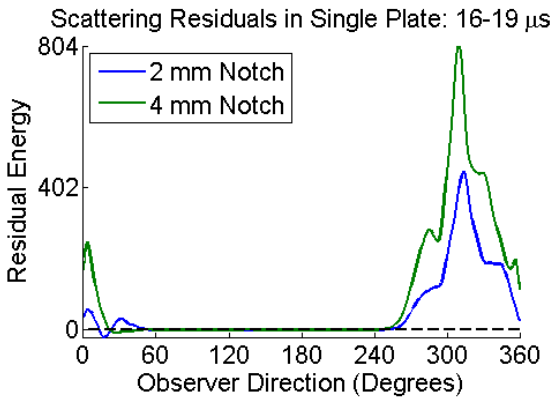

(b)

Figure 5.16: Radial energy analysis for 16-19 μs window in single plate with (a) summed radial energy curves and (b) residual energy

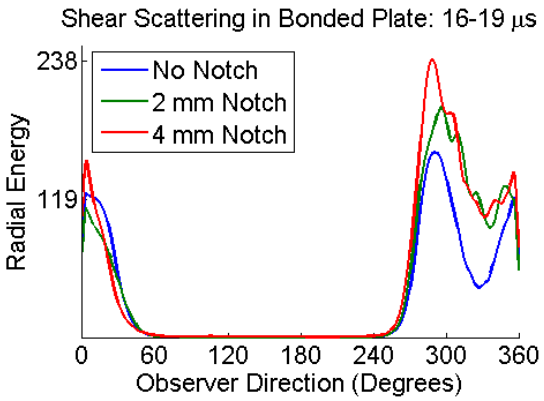

(a)

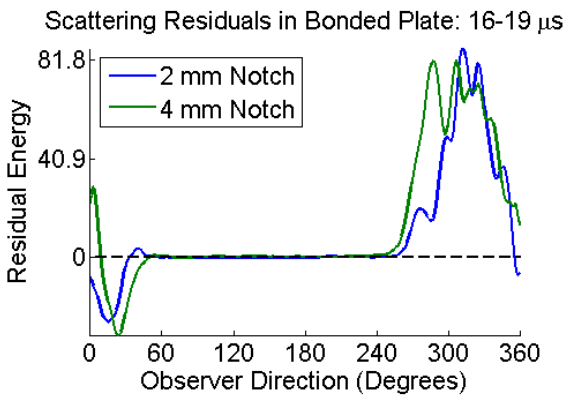

(b)

Figure 5.17: Radial energy analysis for 16-19 μs window in bonded specimen #3 with (a) summed radial energy curves and (b) residual energy

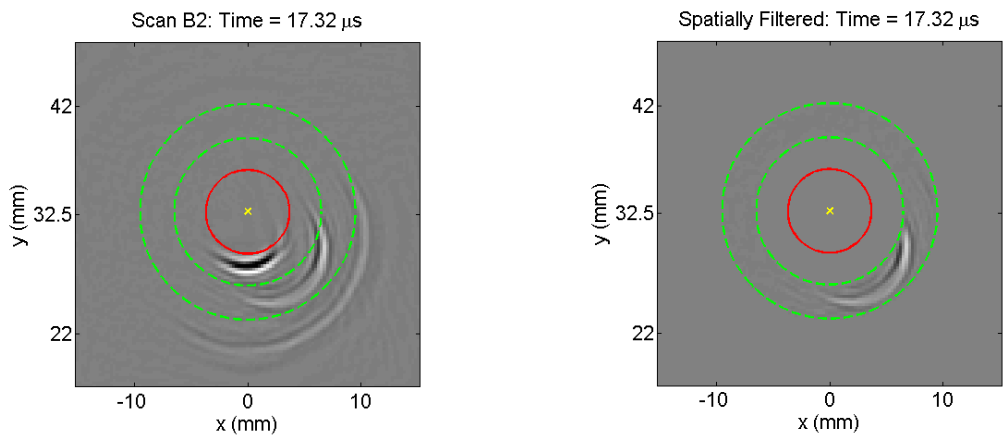

(a) (b)

Figure 5.18: Notch scattering segregation in bonded specimen #1 using an annular spatial window

5.2.5 Space-Windowed Radial Energy

Time-windowed radial energy calculations can also be paired with spatial windowing to further segregate and quantify SOI scattering. Figure 5.18 illustrates a simple spatial window applied to the phase velocity and directional filtered wavefield of the 4 mm notched-hole of bonded specimen #1 (scan B2) before calculating the radial energy for several snapshots via the observer and time-windowed radial energy methodologies. The window spatially restricts energy calculations to the 6.5 mm - 9.5 mm radial distance range so that resulting energy curves represent notch scattering only. It is important to note that some work has been done on time-space tracking filters for windowing particular types of scattering that could, theoretically, be applied to notch-scattered waves [41]. However, this work considers only simple spatial windowing for the application of defect segregation in bonded specimens.

Effectively, the combination of mode filtering, directional filtering, and time-windowed radial energy calculations yields better notch segregation and improved notch scattering quantification results than baseline subtraction. Furthermore, the computation time for the combined filtering techniques is significantly less than the time it takes for a full baseline

subtraction algorithm such as GSTA. A spatial windowing and radial energy processing combination is applied to the first bonded specimen (scans B1 and B2) and second bonded specimen (scans B3 and B4).

Bonded Specimen #1

Snapshot radial energy was calculated at angles from 180° to 360° within an annular window of 3 mm radial width (i.e., the annular spatial window shown in Figure 5.18) for three scattering frames at 16.32 μs, 17.32 μs, and 18.32 μs and for the current and baseline wavefield snapshots, which are shown in the top two rows of Figure 5.19. The calculated radial energy is then used to generate scattering patterns, which are plotted in both polar and rectangular presentations in the bottom two rows of Figure 5.19. For both presentations, the baseline patterns are shown in blue and the current patterns in red. The polar plot helps strengthen intuition of the scattering direction while the rectangular plot allows for a more detailed analysis of the precise angle(s) along which the backscattered shear waves are propagating. The same analysis is performed for both damaged (current) and undamaged (baseline) through-hole wavefields. All results are shown in Figure 5.19, where each column corresponds to the same time frame, and from top-to-bottom are shown frames of the damaged and undamaged through-holes, polar energy plots, and rectangular energy plots, respectively.

At 16.32 μs, the current and baseline wavefields appear to be very similar and consist primarily of the weak backscattered first skip from the through-hole; there is no significant scattering visible from the notch. The energy profile of the current wavefield is close to that of the baseline, yet the radial energy in almost all directions is stronger in the current. The reduction in energy is likely due to epoxy residue in the undamaged through-hole; epoxy filling decreases the reflection coefficient of shear waves incident on the through-hole as discussed in section 2.2.3.

The frame at 17.32 μs clearly shows a notch-scattered wave that reaches its maximum

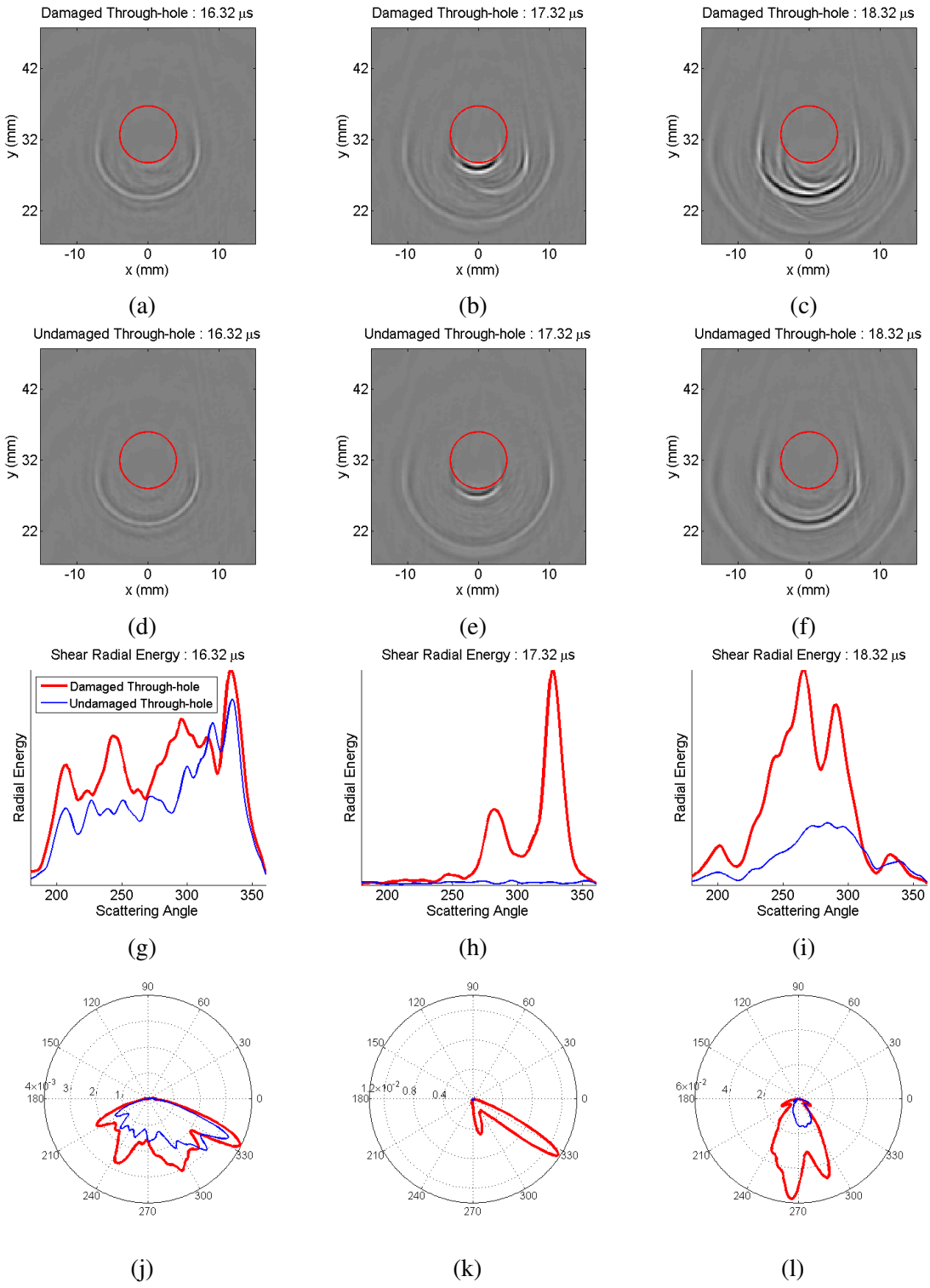

Figure 5.19: Snapshot radial energy methodology applied to multiple frames of damaged (scan B2) and undamaged (scan B1) wavefields

value at an angle of 332° relative to the center of the through-hole. The larger amplitude backscattered second skip from the through-hole is also visible in both the damaged and undamaged through-hole frames. Evidently, the notch-scattered wave, visible in this frame, has resulted from the first incident skip, but has emerged at a shallower angle than that of the nominal notch orientation (28° compared to 45°).

The final frame, at 18.32 μs, shows a second backscattered wave from the notch that is partially overlapped with the backscattered second shear skip from the through-hole. This backscattered wave, which appears to result from the second shear incident skip, has its peak amplitude close to 270°, which is the expected direction of the corner echo. The notch-scattered wave overlaps with the backscattered second shear skip from the hole for propagation directions between 270° and 360°, which likely includes both constructive and destructive interference.

As observed above, the first notch-scattered wave is well-separated from the hole-scattered wave and has its peak at about 332°, whereas the second notch-scattered wave overlaps the hole-scattered wave and the radial energy shows a peak at around 270°. However, the peak at 270° is a combination of the notch- and through-hole backscattered waves, so it cannot be directly attributed to notch scattering. Furthermore, this energy maximum is likely misleading because constructive and destructive interference in the 270° to 360° region may obscure the primary scattering direction of the notch-scattered wave from the second skip. In addition, it would be expected that the second incident shear skip, which is at the nominal refracted angle for a back-surface reflection, should generate a much stronger backscattered wave than the first skip, which is very shallow. This appears to be the case for the hole backscattering but is difficult to confirm for the notch since it is not sufficiently separated from the hole backscattered wave.

Bonded Specimen #2

Recall that the 0.5 skip notch scattering seen in Figure 5.14(b) is physically separated from through-hole scattering, yet directional filtering and snapshot radial energy calculations together yield energy curves and a residual (B4-B3) that contain significantly more through-hole scattering than notch scattering. A simple spatial window can be applied to the C-scan of Figure 5.14(b) to segregate notch scattering from through-hole scattering to yield better notch quantification. Seen in Figure 5.20, an annular spatial window of inner radius 7.5 mm and outer radius 10.5 mm was applied to the phase and directionally filtered wavefields from scans B3 and B4. Notch scattering due to the 0.5 skip incident shear energy is clearly segregated from the rest of the wavefield at 17.6 μs in Figure 5.20 when combining phase velocity, directional, and spatial filtering techniques. Scan B3 is included as baseline data for reference. Figure 5.21(a) shows that notch-scattered energy is clearly dominant in the filtered wavefield; however, the energy curve for B4 is not composed entirely of notch scattering. It is evident from the small negative residual values in Figure 5.21(b) that there remains some minimal scattering energy from the through-hole despite the combination of filtering techniques applied. The residual energy curve shows the contribution of notch scattered energy to the scattering in the fourth ($+x$, $-y$) quadrant of the scattering wavefield. The maximal 0.5 skip notch scattering energy for the 2 mm notch of the second bonded specimen occurs along the 315° (or -45°) direction, which corresponds with the notch orientation for this specimen.

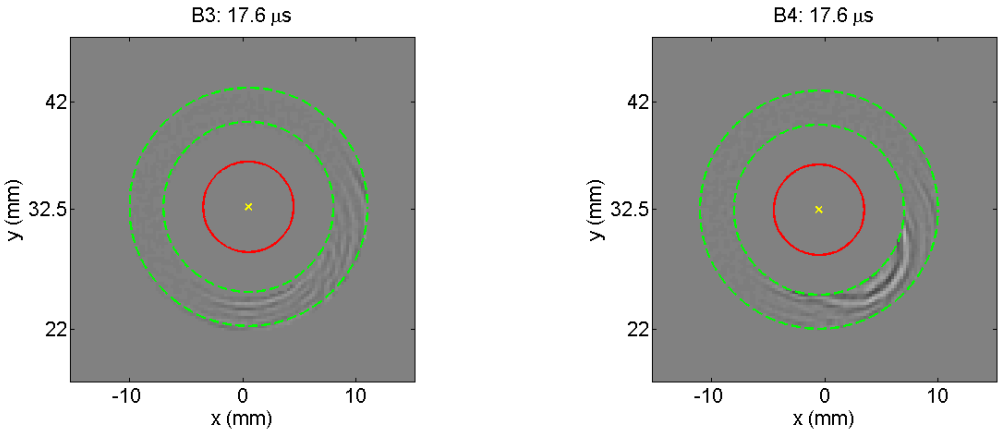

(a) (b)

Figure 5.20: 17.6 μs wavefield frame with spatial window for the undamaged hole (scan B3) and 2 mm notched-hole (scan B4)

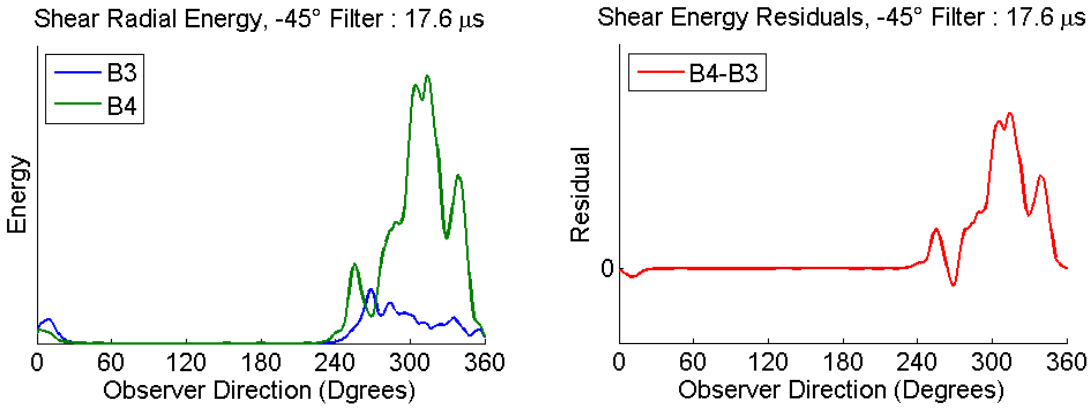

(a) (b)

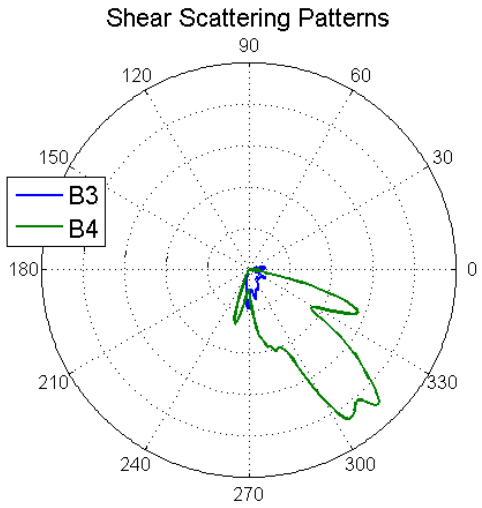

(c)

Figure 5.21: Space-windowed radial energy analysis of bonded specimen #2 with (a) summed radial energy curves, (b) scattering patterns, and (c) residual energy

CHAPTER 6
CONCLUSIONS, DISCUSSION AND RECOMMENDATIONS

This thesis describes the development and implementation of experimental procedures and signal processing techniques to quantify scattering of ultrasonic waves from an element of a buried compound scatterer. Moreover, the scatterer of interest was a buried crack-like defect of variable length emanating from a 6.35 mm diameter through-hole in a bonded 6061 aluminum specimen. Ultrasonic wavefields were measured via wavefield imaging, processed, and analyzed to investigate the effects of notch size and geometry, which are discussed in this chapter. Radial energy curves were developed from prior work [39, 37] to estimate scattering patterns of shear waves in two domains utilizing three methods: full radial energy, snapshot, and windowed calculations.

6.1 Conclusions

This work has shown demonstrable progress on the quantification of ultrasonic shear wave scattering from buried crack-like defects in layered plates. Multiple methods were presented for quantifying notch-scattered waves, and in many cases, scattering was shown to directly correspond with notch orientation. Of the three proposed methods for scattering quantification, windowed radial energy calculations provide the most relevant scattering information and offer metrics for comparing incremental scattering in both time and space. Furthermore, filtering methods for segregating notch scattering from through-hole scattering to yield more accurate notch quantification were presented and applied to measured data for three different bonded specimens. However, scattering in layered plates is complicated, and quantifying scattering from an element of a compound scatterer within layered plates is very difficult due to resulting complexities of the scattering wavefield.

Measuring the wavefield presents more difficulties, as wavefield imaging was shown

to contain a significant amount of undesired low frequency components. Data acquired via wavefield imaging were conditioned to be comparable to typical NDE inspection techniques by applying both time domain and phase velocity filters. Recall that typical NDE inspections, such as pulse-echo or pitch-catch measurements, contain a significant amount of "pre-filtering" of shear waves due to incident and received waves occurring past the first critical angle. However, wave motion here was measured with a broadband LDV on the surface of the specimen, so measured data contained Rayleigh and longitudinal wave components as well as scattering from a broader range of incident angles than would be seen using conventional probes. Furthermore, the ambiguity between shallow-refracted angle shear waves and steep-refracted angle longitudinal waves made it difficult to determine a phase velocity range for filtering shear waves.

In conclusion, this work has largely met its main research objectives and made a contribution to the field of ultrasonic NDE. Wavefield data were obtained for single and bonded plates with through-holes containing notches of incremental length and geometries. In addition, four methods for generating angle-beam scattering patterns for shear wave scattering from 3-D wavefield data were developed and applied.

6.2 Discussion and Recommendations

Although the work covered in this thesis provides a mean of quantifying elemental scattering from a compound scatterer, further work can be done to improve signal processing methods and apply them to wavefield sensitivity experiments to gain more comprehensive understanding of scattering behavior in bonded specimens. The remainder of this chapter is dedicated to further discussing interesting observations from this thesis and providing specific recommendations for future work to improve the signal processing methods described herein and apply them to experiments that are likely to produce meaningful results.

6.2.1 Notch Scattering Segregation

The combination of mode filtering, directional filtering, and windowed radial energy calculations yielded better notch segregation and improved notch scattering quantification results than wavefield baseline subtraction or any of the aforementioned techniques alone. However, this particular processing combination has only been shown to work for the case of notch scattering that is reasonably time-space separated from through-hole scattering. If the notch scattering is physically overlapped with through-hole scattering, then there currently is no practical method of determining how each scatterer contributes to the energy calculation. Furthermore, this is a general consequence of performing scattering analyses in the energy domain as opposed to the time-space domain: phase information that may otherwise be useful to determining the source of scattering is lost when calculating energy curves.

Improvements can also be made to the simple spatial window. For this work, an annular shape centered around the through-hole center was used to window the desired scattering wavefield. Centering the annular window about the notch and through-hole intersection may yield better windowing, as the notch scattering lobe may be more completely contained within the window. The notch scattering was observed to emanate approximately from the notch and through-hole connection point, and since the scattering propagates in a roughly circular pattern, centering a shaped window here should insure that it fits the scattering lobe better.

Two notch geometries were used in this work: a hand-cut corner notch (i.e., used in bonded specimen #1) and electrical discharge machined (EDM) notches with quarter-circular profiles (i.e., used in bonded specimens # 2 and # 3). The variations in experiment conditions among the three bonded specimens, which are summarized in Table 6.1, make it difficult to directly compare scans from different specimens for investigating the effect of either notch geometry or notch orientation.

For instance, data from the first and third bonded specimens are not comparable for

Table 6.1: Summary of experiment conditions for bonded plate scans.

Scan	Notch Type	Length	Orientation	Description
B1	Corner	3 mm	-45°	Good notch-through-hole scattering separation for 0.5 skip ($\sim$17.5 μs)
B4	EDM	2 mm	-45°	Good notch-through-hole scattering separation for 0.5 skip ($\sim$17.5 μs)
B5	EDM	4 mm	-45°	Poor notch-through-hole scattering separation for both 0.5 and 1.5 skips
B7	EDM	2 mm	0°	Poor notch-through-hole scattering separation for both 0.5 and 1.5 skips
B8	EDM	4 mm	0°	Good notch-through-hole scattering separation for 0.5 skip ($\sim$16.5 μs)

determining the effect of notch geometry on notch scattering separation from through-hole scattering because the notches were also at different orientations, which could have additional effects on scattering separation.

The first and second bonded specimens both contained notches at a -45° orientation, but the first bonded specimen notch was 3 mm in length as opposed to the 2 mm and 4 mm notch lengths used in the second bonded specimen. It was observed that notch scattering due to the 0.5 skip was separated from through-hole scattering for the 3 mm notched-hole in bonded specimen #1 and the 2 mm notched-hole in bonded specimen #2 but not the 4 mm notch in bonded specimen #2. Because the notch cross-section and notch lengths were changed from bonded specimen #1 to bonded specimen #2 and increases in notch length do not necessarily imply improved notch scattering separation, it is difficult to attribute separation to either of these notch characteristics. Based on the results from bonded specimen #1 and #2, scattering separation may potentially be more influenced by notch length and orientation rather than notch geometry.

Notch scattering separation was also observed for the 4 mm notched-hole of bonded specimen #3; however, the separation occurs at a different snapshot time, $\sim$16.5 μs, than the separation observed in either bonded specimens #1 or #2.

Attempts to improve notch scattering were also made by altering the probe location and aim point. However, preliminary efforts made to the probe aiming point and distance from the scatterer were found to have little effect on the separation of notch-scattered and through-hole-scattered waves. Work is ongoing to quantify the changes in scattering in response to shifts in probe location.

6.2.2 Half Skip vs. One-and-a-Half Skip Scattering

Throughout section 5.2 distinctions were made between notch scattering from half skip (0.5) incidence energy and one-and-a-half skip (1.5) incident energy. From Figure 5.8, it appeared that it would be much more difficult to quantify notch scattering based on the 1.5 skip as opposed to the 0.5 skip due to overlap with through-hole scattering. Instead, radial energy residuals seen in Figures 5.9(b) and 5.10(b) for the 1.5 skip appear to represent notch scattering behavior. It is important to note that radial energy residuals provide information on the difference between current and reference wavefields, which does not necessarily imply they accurately represent notch scattering behavior alone. Residual energy curves may be skewed by time-space variations between the current and reference wavefields for the snapshot and time-windowed radial energy calculations. However, the sensitivity of residual energy curves to variations in probe location and through-hole scattering were not considered for this work.

1.5 skip incident energy theoretically, but inconclusively in an experimental sense, generates the largest amplitude notch scattering of all skips. This is based on the fact that experiments were designed to generate primary notch scattering from the 1.5 skip, which was incident on the notch at the nominal refracted angle. Instead, this work found that notch scattering due to the 0.5 skip, which coincides with a larger refracted angle (i.e.,

shallower), was more useful for notch scattering quantification because notch scattering was better time-space separated from through-hole scattering. Despite the relatively low amplitude of 0.5 skip notch scattering, reasonable results could still be obtained after the data were filtered and windowed in both the frequency-wavenumber and time-space domains.

Future work should consider the mechanics behind why notch scattering is better physically separated from through-hole scattering for the 0.5 skip than the 1.5 skip. Because wave interactions in the bulk are not recorded when using wavefield imaging to acquire wavefield data, modeling efforts are likely to be useful to understand further the complexities of the scattering behavior at the notch and through-hole intersection point. On the other hand, surface-measured data acquired as a result of this project can be used to validate existing and future models at the surface of layered isotropic specimens.

0.5 skip scattering is not as visible as 1.5 skip scattering in typical pulse-echo measurements because the probe only receives scattering energy near the nominal refracted angle and primarily in the direct backscattering direction (i.e., $-90°$). In contrast, wavefield imaging captures the entire wavefield, including a wider range of refracted angles due to beam spread and forward- and backscattering, so the expectation that the data is dominated by nominal refracted angle backscattering is often not true. Although wavefield imaging allows the opportunity to acquire much more detailed wavefields, it comes at the cost of making direct comparisons to conventional measurements more difficult, and expectations of scattering wavefield behavior may not agree with the reality of an NDE inspector.

6.2.3 Second Bonded Specimen Scattering Behavior

The notch scattering behavior observed in the second bonded specimen is particularly interesting in contrast to the behavior of scattering in the other two specimens because scattering behavior changes significantly between the 2 mm and 4 mm notch cases, despite very similar experimental settings. The exact reason for the significant change in scattering behavior

is not currently known, but the notch length and orientation relative to the incident wave direction could be two potentially significant factors. Modeling efforts in conjunction with experimental data for validation should help improve the ultrasonic testing community's understanding of complicated wave interactions such as these.

6.2.4 Notch Orientation

Although not done in this work, effects of the notch orientation should also be examined. For example, snapshot radial energy curves of scans B3-B5, from the second bonded specimen, could be compared to the radial energy curves of scans B6-B8, from the third bonded specimen, to determine the effect of notch orientation on scattering. Recall that scans B4 and B5 contain notch scattering from notches oriented at -45° with lengths of 2 mm and 4 mm, respectively, and B7 and B8 contain scattering from notches of the same length oriented at 0°. It would be reasonable to expect scattering energy in the B4 and B5 scans would be directed more towards the -45° direction and the energy in scans B7 and B8 directed towards the 0° direction.

This comparison was not made here because the data contained too many non-controlled variables between scans B3-B5 and B6-B8 to make a meaningful comparison. For example, experimental settings, such as the transducer (i.e., transducer A was used for scans B3-B5 and transducer B for scans B6-B8) and probe aim point (i.e., the probe was aimed differently for scans B3-B5 than for scans B6-B8), were changed between acquiring scans B3-B5 and B6-B8. Although the comparison between the -45° and 0° notch orientations was not made directly, observed differences in scattering behavior between the two orientations, such as those discussed in Section 6.2, indicate that it may be beneficial to investigate the effect of notch (or probe) orientation on notch scattering further. The Quantitative Ultrasonic Evaluation Sensing and Testing Laboratory at Georgia Institute of Technology is currently working on wavefield sensitivity studies such as these.

APPENDIX : EXPERIMENT EQUIPMENT

All equipment used for the work completed in this thesis is included below.

- Agilent 33250A (Function Generator)
- Tektronix TDS5034B (Phosphor Oscilloscope)
- Cleverscope CS328A (Digitizer)
- Polytec OFV-5000 Vibrometer Controller (LDV Controller)
- Polytec OFV-551 Fiber Vibrometer (Fiber-optic LDV Head)
- Custom Rexroth/Bosch Group XYZ Translation Stages
- Panametrics 5072PR Pulser/Receiver
- Panametrics ABWM-4T 60° Acrylic Angle-Beam Wedge
- Panametrics 5 MHz $\times$ 0.25" Transducer A (Model # C543-SM, SN 867921)
- Panametrics 5 MHz $\times$ 0.25" Transducer B (Model # C543-SM, SN 1007263)

REFERENCES

[1] L. W. Schmerr Jr., *Fundamentals of Ultrasonic Nondestructive Evaluation*. Springer: Switzerland, 2016.

[2] J. E. Michaels and T. E. Michaels, "An ultrasonic angle beam method for in situ sizing for fastener hole cracks," *Journal of Nondestructive Evaluation*, vol. 25, pp. 3–16, 2006.

[3] M. V. Felice, A. Velichko, and P. D. Wilcox, "Accurate depth measurement of small surface-breaking cracks using and ultrasonic array post-processing technique," *NDT & E International*, vol. 68, pp. 105–112, 2014.

[4] J. Zhang, B. W. Drinkwater, and P. D. Wilcox, "Longitudinal scattering from rough crack-like defects," *IEEE Transactions on Ultrasonics, Ferroelectrics, and Frequency Control*, vol. 62, pp. 549–559, 2015.

[5] J. W. Kummer, A. J. Dawson, J. E. Michaels, and T. E. Michaels, "Effect of fill conditions on bulk wave scattering from a through-hole," *AIP Conference Proceedings*, vol. 1706, no. 1, p. 030 021, 2016.

[6] J. L. Rose, *Ultrasonic Waves in Solid Media*. Cambridge University Press: New York, 1999.

[7] X. Chen, J. E. Michaels, and T. E. Michaels, "Incremental scattering of guided waves from a notch originating at a through-hole," *AIP Conference Proceedings*, vol. 1650, no. 1, pp. 799–806, 2015.

[8] P. Fromme and M. B. Sayir, "Detection of cracks at rivet holes using guided waves," *Ultrasonics*, vol. 40, pp. 199–203, 2015.

[9] P. J. Shull, *Nondestructive Evaluation: Theory, Techniques, and Applications*. Marcel Dekker: New York, 2002.

[10] H. R. Hamidzadeh, D. Liming, and R. N. Jazar, *Wave Propagation in Solid and Porous Half-Space Media*. Springer: New York, 2014.

[11] I. A. Viktorov, *Rayleigh and Lamb Waves: Physical Theory and Applications*. Plenum Press: New York, 1967.

[12] Lord Rayleigh, "On waves propagated along the plane surface of an elastic solid," *Proceedings of the London Mathematical Society*, vol. 1, pp. 4–11, 1885.

[13] O. Mesnil, C. A. Leckey, and M. Ruzzene, "Instantaneous and local wavenumber estimations for damage quantification in composites," *Structural Health Monitoring*, vol. 14, no. 3, pp. 193–204, 2014.

[14] American Society for Nondestructive Testing, *Introduction to Nondestructive Testing*, http://www.olympus-ims.com/en/ndt-tutorials/flaw-detection/applications/, Accessed: 2017-02-20.

[15] Olympus Corporation, *Ultrasonic Flaw Detection Tutorial*, https://www.asnt.org/MinorSiteSections/AboutASNT/Intro-to-NDT, Accessed: 2017-02-20.

[16] T. Hasiotis, E. Badogiannis, and N. G. Tsouvalis, "Application of ultrasonic c-scan techniques for tracing defects in laminated composite materials," *J. Mechanical Engineering*, vol. 57, pp. 192–203, 2011.

[17] A. H. Shah, K. C. Wong, and S. K. Datta, "Surface displacements due to elastic wave scattering by buried planar and non-planar cracks," *Wave Motion*, vol. 7, pp. 319–333, 1985.

[18] J. C. Aldrin and J. S. Knopp, "Modeling and simulation for nondestructive testing with applications to aerospace structures," *Materials Evaluation*, vol. 66, pp. 53–59, 2008.

[19] J. C. Aldrin, M. P Blodgett, E. A. Lindgren, G. J. Steffes, and J. S. Knopp, "Scattering of obliquely incident shear waves from a cylindrical cavity," *Journal of the Acoustical Society of America*, vol. 129, no. 6, pp. 3661–3675, 2011.

[20] C. C. Mow and Y. H. Pao, *The Diffraction of Elastic Waves and Dynamic stress Concentrations*, United States Air Force Project RAND: Tech Rep. #R-482-PR, 1971.

[21] K. F. Graff, *Wave Motion in Elastic Solids*. Dover Publications, 1975.

[22] D. A. Mendelsohn, J. D. Achenbach, and L. M. Keer, "Scattering of elastic waves by a surface-breaking crack," *Wave Motion*, vol. 2, pp. 277–292, 1980.

[23] A. Ilan, L. Bond, and M. Spivak, "Interaction of a compressional impulse with a slot normal to the surface of an elastic half-space," *Geophys J R Astron Soc*, vol. 57, pp. 463–477, 1979.

[24] C. Zhang and J. D. Achenbach, "Scattering of body waves by an inclined surface-breaking crack," *Ultrasonics*, vol. 26, pp. 132–138, 1988.

[25] M. Darmon, V. Dorval, A. K. Djakou, L. Fradkin, and S. Chatillon, "A system for ultrasonic NDT based on the Physical Theory of Diffraction (PTD)," *Ultrasonics*, vol. 6, pp. 115–127, 2016.

[26] M. Darmon, N. Leymarie, S. Chatillon, and S. Mahaut, "Modelling of scattering of ultrasounds by flaws for NDT," CEA LIST, Tech. Rep.

[27] M. Darmon, S. Chatillon, S. Mahaut, P. Calmon, L. Fradkin, and V. Zernov, "Recent advances in semi-analytical scattering models for NDT simulation," *Journal of Physics*, vol. 269, no. 1, 2011.

[28] A. J. Dawson, J. E. Michaels, R. M. Levine, X. Chen, and T. E. Michaels, "Acquisition and analysis of angle-beam wavefield data," *AIP Conference Proceedings*, vol. 1581, no. 1, pp. 1716–1723, 2014.

[29] T. E. Michaels, J. E. Michaels, B. Mi, and M. Ruzzene, "Damage detection in plate structures using sparse ultrasonic transducer arrays and acoustic wavefield imaging," *AIP Conference Proceedings*, vol. 760, no. 1, pp. 938–945, 2005.

[30] Z. Liu, H. Yu, and C. He, "Delamination damage detection of laminated composite beams using air-coupled ultrasonic transducers," *Sci. China Phys. Mech. Astron.*, vol. 56, p. 1269, 2013.

[31] T. E. Michaels, J. E. Michaels, and M. Ruzzene, "Frequency-wavenumber domain analysis of guided wavefields," *Ultrasonics*, vol. 51, pp. 452–466, 2011.

[32] M. Ruzzene, "Frequency-wavenumber domain filtering for improved damage visualization," *Smart Materials and Structures*, vol. 16, pp. 2116–2129, 2007.

[33] Z. Tian and L. Yu, "Lamb wave frequency-wavenumber analysis and decomposition," *Journal of Intelligent Material Systems and Structures*, vol. 25, no. 9, pp. 1107–1123, 2014.

[34] H. Sohn, D. Dutta, J. Y. Yang, M. Desimio, S. Olson, and E. Swenson, "Automated detection of delamination and disbond from wavefield images obtained using a scanning laser vibrometer," *Smart Materials and Structures*, vol. 20, 10pp, 2011.

[35] J. E. Michaels, "Ultrasonic wavefield imaging: Research tool or emerging nde method?" *AIP Conference Proceedings*, vol. 1806, p. 020 001, 2017.

[36] C. T. Maki, J. E. Michaels, Y. Weng, and T. E. Michaels, "Angle-beam shear wave scattering from buried crack-like defects in bonded specimens," *AIP Conference Proceedings*, vol. 1806, p. 020 003, 2017.

[37] A. J. Dawson, *Acquisition and Analysis of Ultrasonic Wavefield Data to Characterize Angle-Beam Propagation and Scattering in Plates*, Georgia Institute of Technology: Ph.D. Thesis, 2016.

[38] A. J. Dawson, J. E. Michaels, and T. E. Michaels, "Isolation of ultrasonic scattering by wavefield baseline subtraction," *Mechanical Systems and Signal Processing*, vol. 70-71, pp. 891–903, 2016.

[39] J. W. Kummer, *Signal Processing Methods to Quantify Scattering of Angle-Beam Shear Waves from Through-holes in Plates*, Georgia Institute of Technology: M.S. Thesis, 2016.

[40] B. S. Reddy and B. N. Chatterji, "An FFT-based technique for translation, rotation, and scale-invariant image registration," *IEEE Transactions on Image Processing*, vol. 5, no. 8, pp. 1266–1271, 1996.

[41] Y. Weng and J. E. Michaels, "Windowing of full wavefield data in multiple domains to characterize angle-beam shear wave scattering," *AIP Conference Proceedings*, vol. 1806, p. 140 007, 2017.